Silent, Solid-State Propulsion for Advanced Air Mobility Vehicles

NIAC Phase I Final Report
February 2023

Team: Prof. Steven R.H. Barrett[1], Arthur Brown[2], Nicolas Gomez-Vega[2]

[1] Professor and Associate Department Head, Department of Aeronautics and Astronautics, Massachusetts Institute of Technology. NIAC Principal Investigator.

[2] Ph.D. Candidate, Department of Aeronautics and Astronautics, Massachusetts Institute of Technology.

Abstract

Propeller-driven uncrewed aircraft for urban and suburban package delivery are in development. These aircraft may be able to deliver packages to customers more quickly and at a lower cost, relative to ground delivery vans with human drivers. However, noise generated by their propellers can annoy local residents, leading to community opposition.

Electroaerodynamic (EAD) propulsion is a novel means of generating thrust without any moving parts, by using strong electric fields to ionize and accelerate air. Because EAD thrusters have no moving parts, they are almost silent in some applications. EAD-powered aircraft may therefore be able to complete urban package delivery missions without community opposition to noise. Multistaged ducted (MSD) thrusters consist of multiple EAD electrode stages enclosed inside a duct. It is shown both theoretically and through experiments that MSD thrusters are more efficient and thrust-dense than their exposed counterparts. This is in part because the duct contributes to thrust, as with ducted fans.

Two MSD-powered uncrewed aircraft configurations are presented: a monoplane and a box wing. Both are capable of vertical takeoff and landing; their MSD thrusters tilt vertically to provide thrust in hover, then tilt horizontally for wingborne flight. They were designed and optimized using a multidisciplinary optimization framework, incorporating a one-dimensional physics-based MSD thruster model, coupled with aerodynamic, structural, weight, and power-electronics models.

While both aircraft concepts can fly a nominal out-and-back urban package delivery mission, their feasibility is contingent on four key technological modeling parameters: thruster ionization energy, stage loss coefficient, power-converter specific power, and battery specific power. Advances in all four areas are required, relative to today’s state-of-the-art. Future work should focus on characterizing and improving these technologies.

Acknowledgements

The authors would like to thank Mihir Shevgaonkar for useful feedback on the power-electronics models and discussions in this work. The authors would also like to thank James (Jamie) Abel and Nicholas Perovich for their assistance with the acoustic measurements.

Nomenclature

A	=	cross-sectional area
b	=	span
C	=	tail volume coefficient
C_d	=	drag coefficient
C_f	=	skin-friction coefficient
C_L	=	lift coefficient
$\bar{c}$	=	mean aerodynamic chord
D	=	drag
D_i	=	induced drag
d	=	gap spacing, or diameter
E	=	energy
e	=	elementary charge
h	=	height
I	=	current
j	=	current density
j_{MG}	=	Mott-Gurney current density
K_L	=	stage loss coefficient
l	=	length
n	=	number of thruster stages
P	=	power, or pressure
p	=	specific power
Q	=	drag interference factor
Re	=	Reynolds number
RMS	=	root mean square
S	=	area
SPL	=	sound pressure level
T	=	thrust
$\frac{t}{c}$	=	thickness-to-chord ratio
V	=	stage DC voltage
v	=	velocity
ΔP	=	total duct pressure rise
$(\Delta P)_{\mathrm{EAD}}$	=	stage EAD pressure rise
$(\Delta P)_{\mathrm{loss}}$	=	stage pressure losses
ε	=	electric permittivity
μ	=	ion mobility
ν	=	kinematic viscosity
ρ	=	air density
ϕ	=	thruster exit area ratio
$\overline{(\ )}$	=	nondimensional property
$(\ )_{\mathrm{accel}}$	=	ion acceleration property
$(\ )_{\mathrm{boom}}$	=	tail or thruster boom property
$(\ )_{\mathrm{box}}$	=	box wing property
$(\ )_e$	=	thruster exit property
$(\ )_{\mathrm{FT}}$	=	forward thruster(s) property
$(\ )_H$	=	horizontal property
$(\ )_{\mathrm{HT}}$	=	horizontal tail property
$(\ )_{\mathrm{HVPC}}$	=	power converter property
$(\ )_{\mathrm{in}}$	=	input property
$(\ )_{\mathrm{ion}}$	=	ion generation property
$(\ )_{\mathrm{out}}$	=	output property
$(\ )_{\mathrm{planar}}$	=	planar wing property
$(\ )_{\mathrm{pod}}$	=	fuselage pod property
$(\ )_{\mathrm{ref}}$	=	reference property
$(\ )_{\mathrm{RMS}}$	=	root mean square
$(\ )_{\mathrm{usable}}$	=	pod usable volume property
$(\ )_V$	=	vertical property
$(\ )_{\mathrm{VT}}$	=	vertical tail property
$(\ )_W$	=	wing property
$(\ )_{\mathrm{wall}}$	=	duct wall property
$(\ )_{\mathrm{wire}}$	=	electrode wire(s) property
$(\ )_1$	=	freestream property
$(\ )_2$	=	duct entrance property
$(\ )_3$	=	duct exit property
$(\ )_4$	=	property far downstream
$(\ )_\infty$	=	freestream property

Table of contents

1 Introduction

1.1 Background: urban package delivery

Advanced air mobility (AAM) is an aviation ecosystem that envisions small crewed and uncrewed aircraft operations, for new or existing applications including intra- and inter-city passenger transport, cargo delivery, and private or recreational operations [1]. One example AAM mission is last-mile package delivery, in which small uncrewed aerial vehicles (UAVs, or drones) deliver packages directly to customers. Wing (a subsidiary of Alphabet), and Amazon Prime Air are among the companies experimenting with UAVs for this application [2], [3]. Hypothesized benefits of such a service, relative to existing ground transportation options such as delivery vans, include [4]–[6]:

- **Greater speed:** UAVs can take direct (as the crow flies) routes and fly over traffic, saving delivery time.
- **Lower cost:** UAVs can be both autonomous and fully electric, saving driver and fuel costs respectively.
- **Lower environmental impact:** UAVs can be fully electric, and therefore (unlike delivery vehicles with internal-combustion engines) do not directly emit greenhouse gases that contribute to climate change. UAVs can even in some cases produce fewer life-cycle greenhouse gases per trip, relative to electric delivery vans [6].

Vehicle noise is a significant obstacle to the widespread adoption of AAM vehicles in general, and to urban package delivery in particular [7], [8]. For example, Wing's drone delivery trials in Canberra, Australia exceeded local noise restrictions, leading to opposition from the local community [9]. A recent drone delivery trial by a different company in Glendale, Arizona encountered community opposition for similar reasons [10]. Propulsion system improvements such as distributed electric propulsion (DEP) could mitigate some noise concerns [11], but fundamental limitations associated with rotating propellers and ducted fans are difficult to overcome without a paradigm shift in propulsion.

1.2 Electroaerodynamic propulsion

Electroaerodynamic (EAD) propulsion is a novel means of generating thrust without any moving parts [12]–[15]. EAD thrusters use strong electric fields to generate and accelerate ions. The ions then generate thrust through collisions with neutral molecules. Previous research has shown that EAD propulsion for fixed-wing aircraft is feasible; i.e., capable of steady level flight [16]. Applications for EAD devices other than propulsion include air purification, flow control, noise reduction, and heat transfer [13], [17], [18].

Because EAD thrusters have no moving parts, they are almost silent in some applications. Aircraft powered by EAD thrusters may therefore be able to complete package delivery missions with reduced community opposition to noise. Preliminary acoustic experiments suggest that EAD thrusters can be 20 dB (two orders of magnitude) quieter than propellers, while producing the same thrust. These experiments are discussed further in Appendix A.

EAD thrusters typically require DC voltages on the order of tens of kilovolts (kV). For example, Xu et al. [16] built and flew the first fixed-wing aircraft to achieve steady level flight while powered entirely by EAD; their aircraft had a thruster voltage of just over 40 kV. This aircraft is hereafter referred to as the V2, or Version 2. A high-voltage power converter (HVPC) is used to increase the voltage from the relatively low voltage available from onboard batteries (typically up to hundreds of volts) to the higher voltage required by the thrusters. The design of the HVPC used in the Xu et al. flights is described by He et al [19].

The historic weakness of EAD propulsion for fixed-wing aircraft propulsion is thrust density (thrust per unit cross-sectional area). Thrust densities measured from EAD experiments have been 3–4 orders of magnitude lower than those of aircraft turbofan engines, and about half as large as those of UAV propellers [15]. This limitation can be partially overcome with multistaged ducted (MSD) EAD thrusters, in which multiple EAD electrode stages are enclosed inside a duct [20]. MSD thrusters are both more powerful and more efficient than their exposed counterparts. This is in part because the duct contributes to thrust, as is the case in ducted fans. Other hypothesized advantages of MSD thrusters include:

- The duct can support the electrodes, so they can be made smaller, reducing drag losses.
- By using multiple small stages instead of one large thruster, the power-converter output voltage can be lowered; the power-converter mass can therefore be reduced.
- The duct can act as a physical barrier between the electrodes and the surroundings, increasing safety.
- The duct can serve as an acoustic liner, further reducing noise.

Sample experimental data for a single-stage ducted thruster, demonstrating its advantages relative to an equivalent unducted system, is provided in Appendix B.

1.3 Project goals

The primary goal of this study is to design a family of uncrewed aircraft, powered by MSD EAD thrusters, for a package delivery mission. The aircraft will be capable of vertical takeoff and landing (VTOL). Unlike propeller drones, the aircraft will be nearly silent, potentially enabling package delivery missions in noise-sensitive areas (e.g., suburbs) without community noise opposition. This mission is depicted in Figure 1. A secondary goal is to identify parameter and modeling sensitivities, solutions to which will be required to build and fly the aircraft.

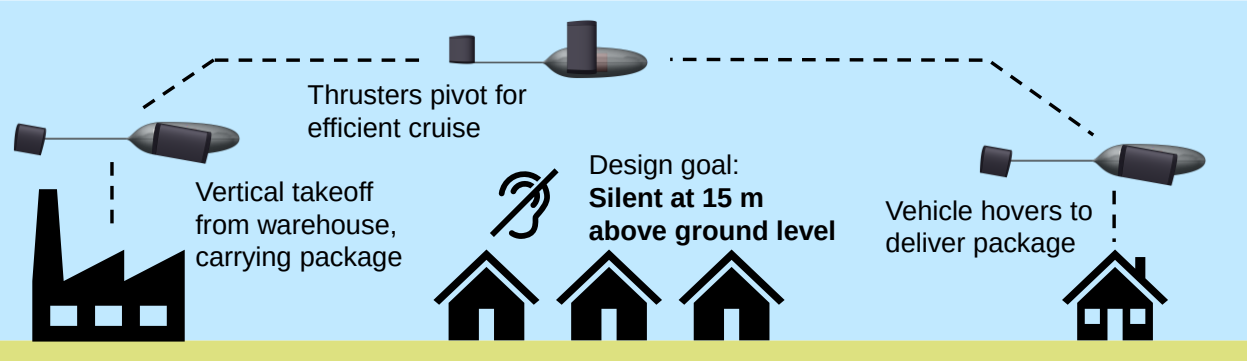

Figure 1: Proposed mission for the EAD VTOL package-delivery aircraft.

The rest of this report is structured as follows. The study methods, including mission requirements, aircraft concepts, design optimization algorithm, and thruster, power-electronics, and aircraft models, are given in Section 2. Results, sensitivity analyses, and discussion are given in Section 3, before the conclusion in Section 4.

2 Methods

2.1 Mission requirements

As mentioned in Section 1.1, Wing and Prime Air are experimenting with using uncrewed aircraft to deliver packages. Characteristics of their aircraft concepts, taken from [2], [21] and other sources, are given in Table 1.

Table 1: Characteristics of package delivery aircraft in development.

		Wing	**Prime Air**
Vehicle	Configuration	Lift + cruise	Tail sitter
	Mass	6.4 kg	40.4 kg
Payload	Dimensions	22.9 cm × 17.8 cm × 15.2 cm	45.7cm × 35.6cm × 20.3cm
	Mass	1.2 kg	2.8 kg
	Carriage	Cardboard fairing	Internally carried box
	Delivery	Lowered via winch	Dropped at low altitude
Mission	Radius	10 km	24 km
	Speed	29 m/s	20+ m/s

Based on Table 1, the following requirements were selected for the aircraft in this study:

- **Payload mass of 1.2 kg.** This is the same as for Wing.
- **Payload dimensions of 22.9 cm × 17.8 cm × 15.2 cm** (length × width × height). Wing's vehicle is often depicted carrying food as its payload [2]. These dimensions are sufficient to carry either two 20 fl. oz. (591 mL) coffee cups end-to-end [22], or any of the standard sizes of folded cardboard take-out food boxes [23].
- **Payload carried internally,** as with Amazon Prime Air. This is mainly done to reduce drag; it may also prevent the thrusters from causing surface charging of the payload.
- **Mission radius of 10 km.** The vehicle must fly 10 km out to a customer, drop the payload, then fly 10 km back. This is the same radius as for Wing.

The optimization is agnostic to payload delivery mechanism (lowered via winch vs. dropped at low altitude). Instead, the payload mount weighs a fixed fraction of the payload mass (see Section 2.6). No constraints on flight speed are imposed. The mission profile is summarized in Table 2.

Table 2: Mission profile, showing the requirements for each mission segment.

Mission segment	**Requirements**
Takeoff	5 s in hover.
Climb	Minimum climb rate of 1.52 m/s.
Cruise out	10 km in wingborne flight.
Payload drop	20 s in hover.
Turn around	180° turn in wingborne flight; 30° bank angle.
Cruise in	10 km in wingborne flight.
Landing	5 s in hover.

Table 2 shows two types of mission segment: hover segments (takeoff, payload drop, and landing), and wingborne segments (climb, cruise out, turn, and cruise in). All hover segments require the total thrust to be at least 10% greater than the vehicles' mass, accounting for both control margins and suckdown effects [24]. Meanwhile, all wingborne flight segments must be flown at an airspeed at least 20% greater than the stall speed.

2.2 Aircraft concepts

Two design concepts were selected: a monoplane and a box wing. To-scale sketches of both concepts were generated using Open Vehicle Sketch Pad (OpenVSP) [25]. Isometric views of the monoplane in wingborne flight and in hover are provided in Figure 2 and Figure 3 respectively; additional views are in Appendix C.

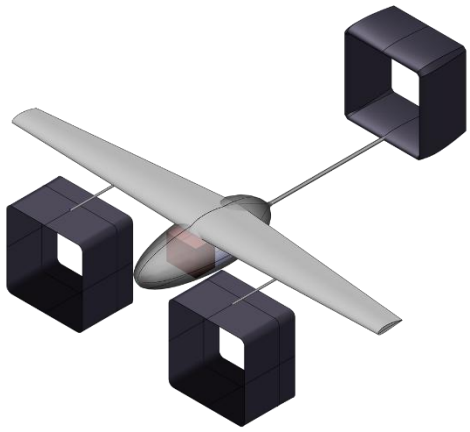

Figure 2: Isometric view of the monoplane in wingborne flight.

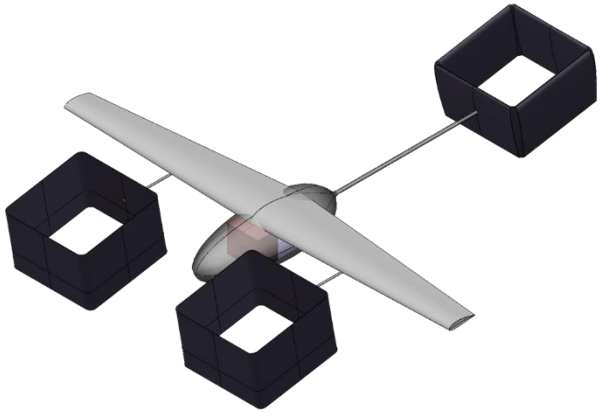

Figure 3: Isometric view of the monoplane in hover.

The monoplane consists of a fuselage pod, wing, and tail boom. It also has three MSD thrusters, depicted in black. In Figure 2, the thrusters are level, providing thrust in wingborne flight; in Figure 3, the thrusters tilt, providing lift in hover.

The first thruster is at the rear of the airplane. It also serves as the tail; i.e., it provides stability, and has an elevator and rudder for control. The two remaining thrusters (hereafter called the forward thrusters) are located under each wing, and are offset forward of the wing by forward booms. This offset serves to position them forwards of the aircraft center of gravity (CG), so that the aircraft thrust balances in hover.

Isometric views of the box wing in wingborne flight and in hover are provided in Figure 4 and Figure 5 respectively; additional views are in Appendix C.

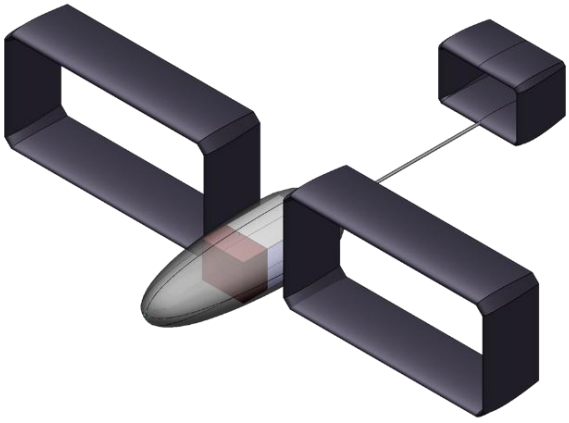

Figure 4: Isometric view of the box wing in wingborne flight.

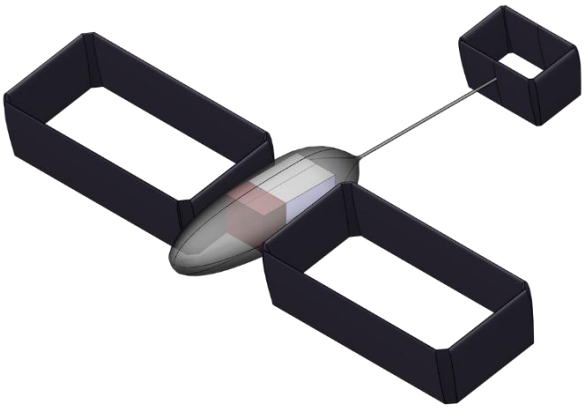

Figure 5: Isometric view of the box wing in hover.

Like the monoplane, the box wing consists of a fuselage pod, tail boom, and box-tail thruster. However, instead of a conventional wing and two forward thrusters, the box wing doubles as a thruster. The box wing tilts forwards in hover, so that its thrust vector is forwards of the CG, ensuring the aircraft balances.

2.3 Design optimization algorithm

The aircraft were designed using signomial programming (SP), a multidisciplinary design optimization algorithm. Signomial programs are faster and more robust than general nonlinear optimization algorithms [26]. However, the objective function and constraints must be formulated as monomial, posynomial, and signomial functions; black-box models cannot be directly used. Signomial programming (as well as geometric programming [27], a simplification of SP) has been applied to the design and optimization of high-altitude communications and surveillance aircraft, urban air taxis, short-takeoff-and-landing (STOL) aircraft, airliners, and electric propulsion systems [28]–[35].

Takeoff mass (minimize) was selected as the objective function. Optimization data, including number of free variables, constraints, and typical optimization solve times is provided in Table 3.

Table 3: Number of free variables, number of constraints, and typical solve times on a laptop computer.

	Monoplane	**Box wing**
Free variables	1663	1525
Constraints	3339	3063
Typical solve time	1.0 s	2.9 s

2.4 Thruster models

The MSD thruster designs presented in this work are modeled by adapting the one-dimensional (1D) ideal MSD thruster model from Gomez-Vega et al [20]. The equations used are repeated here for convenience.

A diagram of an MSD thruster is shown in Figure 6. It consists of an inlet, a duct with constant cross-sectional area that contains multiple stages of EAD electrodes, and a nozzle. The numbered stations (vertical dotted lines) are referenced by the thruster model. A single MSD thruster stage is shown in Figure 7. It consists of an emitter and a collector electrode, separated by a gap spacing, with an applied DC voltage. Electrode geometry is discussed further in Section 2.7.2.

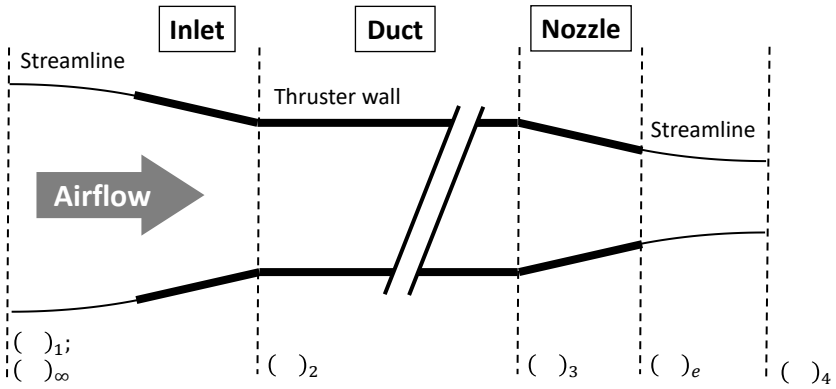

Figure 6: Side-view diagram of an MSD thruster, showing the inlet, duct, and nozzle.

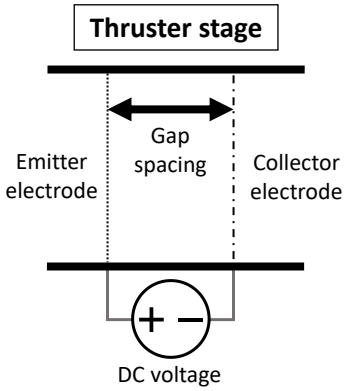

Figure 7: Side-view diagram of one MSD thruster stage.

Modeling approximations are as follows. The flow is assumed to be steady-state and quasi-one-dimensional (1D); current is limited by space charge. Geometry and performance of the inlet, as well as interference between electrodes, is neglected. The duct area is constant between stations 2 and 3, and the duct exit pressure is assumed to be atmospheric. Finally, the stage pressure rise and losses are assumed to be independent of the number of stages (i.e., identical for each stage).

Under these conditions, simple momentum theory can be used to predict the overall thruster behavior. The equations used are Equations 2–4, 9, and 41 from Ref. [20], repeated here as

$$v_2 = \frac{A_e}{A_2} v_4 = \phi v_4 \tag{1}$$

$$v_4 = \sqrt{v_\infty^2 + 2\frac{\Delta P}{\rho}} \tag{2}$$

$$\frac{T}{A_2} = \rho v_4 (v_4 - v_\infty)\phi - \frac{D_{\text{wall}}}{A_2} \tag{3}$$

$$(\Delta P)_{\text{loss}} = \frac{1}{2}\rho v_2^2 K_L \tag{4}$$

$$\Delta P = n[(\Delta P)_{\text{EAD}} - (\Delta P)_{\text{loss}}] \tag{5}$$

where $v_1 = v_\infty$ is the freestream velocity, $v_2 = v_3$ is the thruster bulk velocity, $v_4 = v_e$ is the exit velocity, $\phi = \frac{A_e}{A_2}$ is the exit area ratio (exit cross-sectional area / duct cross-sectional area), ΔP is the duct pressure rise between stations 2 and 3, ρ is the air density, $\frac{T}{A_2}$ is the thrust density, $(\Delta P)_{\text{loss}}$

is the stage pressure loss, K_L is the stage loss coefficient, n is the number of thruster stages[‡], and $(\Delta P)_{\mathrm{EAD}}$ is the stage pressure rise due to EAD. Equation (3) is an extension of Equation 4 from Ref. [20]: inner wall drag D_{wall} is added, to account for losses due to friction from the inside of the duct walls.

The stage pressure rise due to EAD is obtained using Equations 12, 21, and 22 from Ref. [20], repeated here as

$$\overline{(\Delta P)_{\mathrm{EAD}}} \equiv \frac{\mu(\Delta P)_{\mathrm{EAD}}}{j_{\mathrm{MG}} d} \tag{6}$$

$$\overline{v_2} \equiv \frac{v_2 d}{\mu V} \tag{7}$$

$$j_{\mathrm{MG}} = \frac{9}{8}\varepsilon\mu\frac{V^2}{d^3} \tag{8}$$

$$\overline{(\Delta P)_{\mathrm{EAD}}} = (1+\overline{v_2})\left(1-\frac{\overline{v_2}}{3}\right) \tag{9}$$

where $\overline{(\Delta P)_{\mathrm{EAD}}}$ is the nondimensional stage pressure rise due to EAD, μ is the ion mobility, d is the thruster stage gap spacing (distance between emitter and collector electrodes), $\overline{v_2}$ is the nondimensional thruster bulk velocity, V is the stage applied DC voltage, j_{MG} is the Mott-Gurney current density, and ε is the electric permittivity.

Next, the current density is obtained using Equations 15-16 from Ref. [20], repeated here as

$$\bar{j} \equiv \frac{j}{j_{\mathrm{MG}}} \tag{10}$$

$$\bar{j} = (1+\overline{v_2})^2 \tag{11}$$

where $\bar{j}$ is the nondimensional current density, and j is the current density.

Duct inner wall losses are estimated using an equivalent skin-friction method, given here as

$$\mathrm{Re}_{\mathrm{wall}} = \frac{v_2 l_{\mathrm{thruster}}}{\nu} \tag{12}$$

$$C_f = \frac{0.074}{\mathrm{Re}_{\mathrm{wall}}^{0.2}} \tag{13}$$

$$D_{\mathrm{wall}} = \frac{1}{2}\rho v_2^2 S_{\mathrm{wall}} C_f Q_{\mathrm{wall}} \tag{14}$$

where $\mathrm{Re}_{\mathrm{wall}}$ is the wall Reynolds number, l_{thruster} is the thruster nacelle length, ν is the kinematic viscosity, C_f is the skin-friction coefficient, S_{wall} is the wall inner surface area, and Q_{wall} is an interference factor. Equation (13) is the skin-friction coefficient of a turbulent flat plate, as given by Hoburg & Abbeel [27].

[‡] For the purpose of design optimization, number of thruster stages is approximated as a continuous variable, rather than as an integer.

Finally, the power density (electrical power from the power converter / duct cross-sectional area) is obtained using

$$\frac{P}{A_2} = \left(\frac{P}{A_2}\right)_{\text{ion}} + \left(\frac{P}{A_2}\right)_{\text{accel}} \tag{15}$$

$$\left(\frac{P}{A_2}\right)_{\text{ion}} = \frac{njE_{\text{ion}}}{e} \tag{16}$$

$$\left(\frac{P}{A_2}\right)_{\text{accel}} = njV \tag{17}$$

where $\frac{P}{A_2}$ is the electrical power density, the subscripts $(\quad)_{\text{ion}}$ and $(\quad)_{\text{accel}}$ refer to ion generation and ion acceleration respectively, E_{ion} is the amount of energy required to generate one ion, and e is the elementary charge.

Equations (2), (3), (5), (9), (11), and (15) are not solved in their respective forms, as given above. Instead, they are rearranged. This is discussed further in Appendix D.

Unless otherwise specified, the MSD thrusters in this study are modeled using the parameters in Table 4. Standard sea-level values for air density and kinematic viscosity are used (not tabulated), while electric permittivity assumes that the values for air and for a vacuum are the same [36]. Ion mobility was obtained from Ref. [37], and is also consistent with EAD thruster experiments conducted by the authors [38]. MSD thruster experiments by the authors have used a gap spacing of 10 mm. Ionization energy and stage loss coefficient are discussed further in Sections 3.2 and 3.3 respectively. Finally, Table 4 includes upper limits on voltage and exit area ratio. The former limit is included to prevent the thrusters from sparking (arcing), while the latter limit prevents flow separation in the nozzle.

Table 4: Thruster model parameter values.

Parameter	Symbol	Value
Electric permittivity	ε	$8.85 \times 10^{-12}\,\frac{\text{F}}{\text{m}}$
Ion mobility	μ	$2.0 \times 10^{-4}\,\frac{\text{m}^2}{\text{s V}}$
Elementary charge	e	$1.6 \times 10^{-19}\,\text{C}$
Gap spacing	d	10 mm
Ionization energy	E_{ion}	66 eV
Stage loss coefficient	K_L	2.0×10^{-3}
Wall friction interference factor	Q_{wall}	1.1
Maximum applied voltage	V_{max}	10 kV
Maximum exit area ratio	ϕ_{max}	1.0

2.5 Power electronics models

The power-electronics system consists of two components: the battery, and the power converter (which converts the battery output to higher voltages for the thrusters). Sizing parameters for both components are given in Table 5.

Table 5: Power-electronics sizing parameters.

Parameter		Value
Battery	Specific energy	$200\,\frac{\mathrm{W\,h}}{\mathrm{kg}}$
	Specific power	$4\,\frac{\mathrm{kW}}{\mathrm{kg}}$
	Density	$2.4\,\frac{\mathrm{kg}}{\mathrm{L}}$
Power converter	Specific power	$10.3\,\frac{\mathrm{kW}}{\mathrm{kg}}$
	Efficiency	85%

The battery was sized using a fixed specific energy, specific power, and density. The specific energy (200 Wh/kg) is consistent with existing prototype lithium-ion batteries [39]. However, the specific power (4 kW/kg) is about twice that of existing batteries. This choice is discussed further in Section 3.5.

The power converter was sized using a fixed specific power[§] and efficiency. The efficiency (85%) is consistent with that of the power converter used in the Xu et al. flights [16], [19]; however, the specific power (10.3 kW/kg) is approximately ten times higher. This choice is discussed further in Section 3.4.

2.6 Aircraft mass, drag, & structural models

Aircraft-level sizing parameters are summarized in Table 6. Induced drag is estimated using a constant span efficiency; the box wing includes an adjustment for interference between wings (see Appendix E). 10% margins on mass and drag at the aircraft level (in addition to component margins) are maintained.

Table 6: Aircraft sizing parameters.

Parameter	Value
Aircraft mass margin	10%
Aircraft drag margin	10%
Wing span efficiency	0.8
Wing maximum lift coefficient	1.5

[§] Specific power is defined as device output power divided by mass.

Mass models for most aircraft components are based on a bottom-up summation approach, using component dimensions and material densities. If a component is made of composites (either carbon fiber or Kevlar), its material density is doubled, a rule of thumb that accounts for resin mass. Components with structural models are sized using engineering beam theory. If the component is an airfoil, profile drag is estimated using a fit to airfoil data from XFoil [40]; if not, profile drag is estimated using an equivalent flat-plate approach, as described by Raymer [24].

Nacelle components with thrusters inside have drag losses divided into two components. Drag from the outside of the component (facing the freestream) is modeled as profile drag, and is described in this section. Drag from the inside of the component (facing the thruster electrodes) is modeled as a thrust loss, and was previously described in Section 2.4.

Aircraft component mass, profile drag, and structural models are summarized in Table 7. Further modeling details specific to the box wing are discussed in Appendix E.

Table 7: Mass, profile drag, and structural models.

Component	Mass model	Profile drag model	Structural model
Fuselage pod	Kevlar skin (2 plies); 50% mass margin for internal structure.	Equivalent turbulent flat-plate drag with a form-factor adjustment [24]. 20% interference factor.	n/a
Tail boom	Hollow Kevlar cylindrical tube; 10% mass margin.	Equivalent turbulent flat-plate drag. No interference factor.	Cantilever load from tail-thruster thrust in hover. Bending, shear, and tip-deflection (max 5% of boom length) constraints. Factor of safety of 3.
Monoplane wing	Carbon-fiber spar caps & shear web; foam spar core; Kevlar skin (1 ply). 20% mass margin.	Fit to NACA 44XX airfoil data: $C_d = f\left(\frac{t}{c}, \mathrm{Re}, C_L\right)$. Fit RMS error: 1.8%. 20% interference factor.	Loads from a symmetric pull-up at cruising speed, with a load factor of 2.5. Constant beam curvature [41]. Bending, shear, and tip-deflection (max 5% of wingspan) constraints. Factor of safety of 1.5.
Box-wing horizontal section	Same as monoplane wing.	Fit to NACA 44XX airfoil data: $C_d = f\left(\frac{t}{c}, \mathrm{Re}, C_L\right)$. Fit RMS error: 4.3%. 20% interference factor.	Same as monoplane wing, with the upper & lower sections each carrying 50% of the lift.
Box-wing vertical section	Kevlar skin (1 ply); foam spar (10% of section chord). 20% mass margin.	Fit to NACA 00XX airfoil data: $C_d = f\left(\frac{t}{c}, \mathrm{Re}\right)$. Fit RMS error: 1.6%. 20% interference factor.	n/a

Box wing	2 horizontal sections + 4 vertical sections. 30% mass margin.	Inherited from monoplane wing and vertical sections. 20% interference factor.	Inherited from monoplane wing.
Box tail	Kevlar skin (1 ply); foam core. 20% mass margin.	Fit to NACA 00XX airfoil data: $C_d = f\left(\frac{t}{c}, \mathrm{Re}\right)$. Fit RMS error: 2.3%. 10% interference factor.	n/a
Forward thruster nacelles (monoplane only)	Kevlar skin (2 plies). 50% mass margin for structure.	Equivalent flat-plate drag, assuming the flow trips (becomes turbulent) at the nozzle. 20% interference factor.	n/a
Forward thruster booms (monoplane only)	Hollow Kevlar cylindrical tubes; 10% mass margin.	Equivalent turbulent flat-plate drag. No interference factor.	Cantilever load from forward-thrusters thrust in hover. Bending, shear, and tip-deflection (max 5% of boom length) constraints. Factor of safety of 3.
Landing gear	4% of aircraft unmargined mass.	5% of aircraft unmargined profile drag.	n/a
Payload mount	25% of payload mass.	n/a	n/a
Battery	Fixed specific energy, power, and volume (see Section 2.5).	n/a	n/a
Thrusters	Grid of tungsten wires (see Section 2.7.2).	Modeled as a thrust loss rather than drag, via the loss coefficient (Section 2.4).	n/a
Thruster tilting mechanisms	25% of respective thruster + nacelle mass.	n/a	n/a
Avionics	2% of aircraft unmargined mass.	n/a	n/a

2.7 Dimensional models

2.7.1 Fuselage pod

The purpose of the fuselage pod is to hold the battery, payload, power converter, and avionics. A cutaway of the monoplane fuselage pod is shown in Figure 8. The box wing uses a similar design.

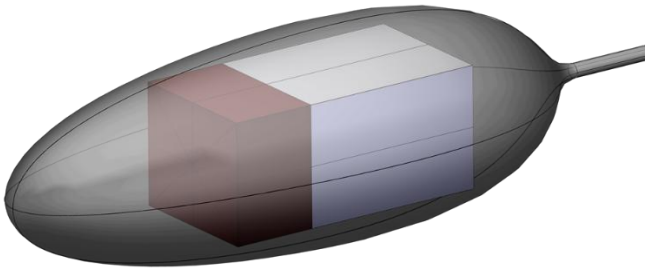

Figure 8: A cutaway of the monoplane fuselage pod.

The fuselage pod is shaped like an ellipsoid, with a length, width, and height. Figure 8 shows the battery (red) and the payload (blue). Both of these components are shaped like rectangular prisms. The battery length, width, and height are optimization variables; its volume is modeled via its density (see Table 5). Payload dimensions are discussed in Section 2.1.

In order to ensure that the battery and payload fit inside the fuselage pod, a "usable volume" is defined. The usable volume is shaped like a rectangular prism; the battery and payload must fit inside it. The usable volume is modeled by enforcing the constraint

$$1 \geq \left(\frac{l_{\text{usable}}}{0.95 l_{\text{pod}}}\right)^2 + \left(\frac{w_{\text{usable}}}{0.95 w_{\text{pod}}}\right)^2 + \left(\frac{h_{\text{usable}}}{0.95 h_{\text{pod}}}\right)^2 \tag{18}$$

where l, w, and h refer to length, width, and height respectively. The subscripts $(\ )_{\text{pod}}$ and $(\ )_{\text{usable}}$ refers to the fuselage pod and usable volume respectively; the factor of 0.95 is a margin.

Since the payload and battery are aligned lengthwise, the sum of their lengths must not exceed the usable fuselage-pod length. This is enforced via the constraint

$$l_{\text{usable}} \geq l_{\text{battery}} + l_{\text{payload}} \tag{19}$$

Finally, battery and payload width and height constraints are defined as

$$w_{\text{usable}} \geq w_{\text{battery}} \tag{20}$$
$$w_{\text{usable}} \geq w_{\text{payload}} \tag{21}$$
$$h_{\text{usable}} \geq h_{\text{battery}} \tag{22}$$
$$h_{\text{usable}} \geq h_{\text{payload}} \tag{23}$$

The avionics system and power converter lack volume models, and are therefore not shown in Figure 8. However, Figure 8 shows that there is still plenty of room in the fuselage. Therefore, the avionics system is located in the nose (in front of the battery), while the power converter is located behind the payload. These assumptions are used for center-of-gravity analysis (see Appendix F).

2.7.2 Thrusters & nacelles

The thruster electrodes are modeled as a grid of cylindrical wires, as shown in Figure 9.

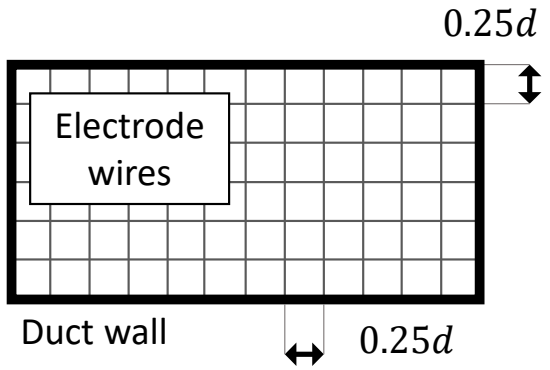

Figure 9: Front view of an MSD thruster duct, showing the electrode geometry.

The grid wires are made of tungsten, and are 56 microns in diameter. Wires with these properties have been used as emitter electrodes in ongoing MSD thruster experiments conducted by the authors (Appendix B). The spacing between wires, as shown in Figure 9, is defined as 25% of the gap spacing (i.e., 2.5 mm in this example). Two grids are required per stage: one grid for the emitters, and one for the collectors. Whether this geometry would work in practice is uncertain.

The thruster stage length is then defined as 20% greater than the stage gap spacing, a margin added to avoid counter-ionic wind [20]. The duct length is the sum of the lengths of the individual stages. Finally, the nozzle length is defined as 20% of the duct length.

The box tail and monoplane forward-thruster nacelles lack structural models (see Table 7). Instead, an upper limit on nacelle aspect ratio is imposed.

Sizing parameters for the thrusters and nacelles are summarized in Table 8.

Table 8: Thruster and nacelle model parameter values.

Parameter	Value
Electrode wire spacing	25% of stage gap spacing
Electrode wire diameter	56 microns
Thruster stage length	20% greater than gap spacing
Thruster nozzle length	20% of duct length
Nacelle maximum aspect ratio	1.5

2.7.3 Box tail

Both the monoplane and box wing include a box tail, which serves two purposes. Firstly, the box tail provides static stability and control (via control surfaces) in wingborne flight. Secondly, it houses a thruster that provides thrust in both hover and wingborne flight.

A minimum tail size for static stability in wingborne flight is defined using tail volume coefficients [24] as

$$C_{\mathrm{HT}} \leq \frac{l_{\mathrm{HT}} S_{\mathrm{HT}}}{b_W S_W} \tag{24}$$

$$C_{\mathrm{VT}} \leq \frac{l_{\mathrm{VT}} S_{\mathrm{VT}}}{\bar{c} S_W} \tag{25}$$

where C is the tail volume coefficient, l is the tail moment arm, S is the planform area[**], b_W is the wingspan, and $\bar{c}$ is the wing mean aerodynamic chord. The subscripts $(\ \ )_W$, $(\ \ )_{\mathrm{HT}}$, and $(\ \ )_{\mathrm{VT}}$ refer to the wing, horizontal tail, and vertical tail respectively.

Equations (24)-(25) can be directly applied to the box wing. However, the monoplane's forward thrusters have a destabilizing influence, since they are located forwards of the aircraft center of gravity (see Appendix E). This is accounted for by extending equations (24)-(25) to obtain

$$C_{\mathrm{HT}} + \frac{2 l_{\mathrm{FT}} (S_H)_{\mathrm{FT}}}{b S_W} \leq \frac{l_{\mathrm{HT}} S_{\mathrm{HT}}}{b S_W} \tag{26}$$

$$C_{\mathrm{VT}} + \frac{2 l_{\mathrm{FT}} (S_V)_{\mathrm{FT}}}{b S_W} \leq \frac{l_{\mathrm{VT}} S_{\mathrm{VT}}}{\bar{c} S_W} \tag{27}$$

where the subscript $(\ \ )_{\mathrm{FT}}$ refers to the forward thrusters, and $(S_H)_{\mathrm{FT}}$ and $(S_V)_{\mathrm{FT}}$ are the total forward-thruster horizontal and vertical planform areas respectively. A factor of 2 is included, because the monoplane has two forward thrusters.

The box tail lacks a structural model (see Table 7). However, it is also a thruster nacelle, and so it is subject to the same constraint on maximum aspect ratio as for the monoplane forward-thruster nacelles (see Section 2.7.2).

Tail volume coefficients are provided in Table 9. They are identical to those used by Burton & Hoburg [28].

Table 9: Tail volume coefficients.

Component	Volume coefficient
Horizontal tail	0.45
Vertical tail	0.04

[**] The box wing planform area S_W is the sum of the planform areas of the upper and lower surfaces. The horizontal-tail planform area S_{HT} is the sum of the planform areas of the upper and lower box-tail surfaces. Finally, the vertical-tail planform area S_{VT} is the sum of the planform areas of the left and right box-tail surfaces.

3 Results

3.1 Design optimization results

A summary of the optimization results is provided in Table 10. Isometric views of both vehicles were provided in Section 2.2; additional views are provided in Appendix C. Detailed dimensional data, mass breakdowns, and detailed performance data for both vehicles are provided in Appendix G, Appendix H, and Appendix I respectively.

Table 10: Summary of the design optimization results.

	Monoplane	**Box wing**
Length	1.62 m	1.51 m
Wingspan	2.21 m	1.60 m
Wing area	0.492 m^2	0.772 m^2
Takeoff (total) mass	20.8 kg	18.6 kg
Payload mass	1.2 kg	1.2 kg
Battery mass	7.5 kg	6.7 kg
HVPC mass	2.5 kg	2.2 kg
Cruising speed	25.5 m/s	25.2 m/s
Cruise lift coefficient	1.04	0.60
Cruise drag coefficient	1019 counts	607 counts
Cruise lift-to-drag	10.2	10.0
Max electrical power	29.9 kW	26.8 kW

Mass and cruise drag breakdowns are provided in Figure 10 and Figure 11 respectively. Note that only the monoplane has forward nacelles and booms; the box wing lacks these components.

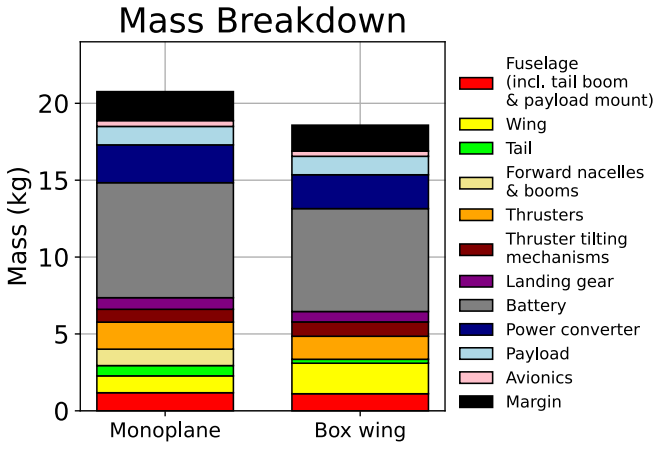

Figure 10: Mass breakdown.

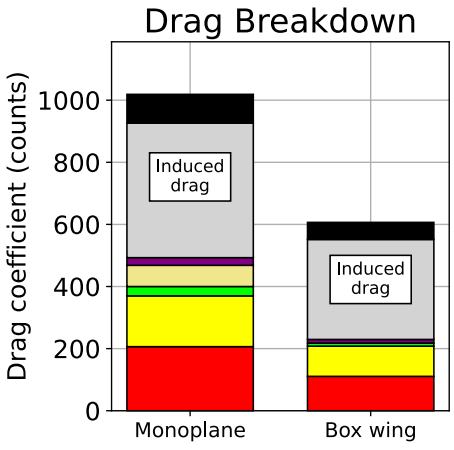

Figure 11: Drag breakdown in cruise.

Figure 10 shows that the battery accounts for the single greatest fraction of the mass: 36% for both vehicles. The second-heaviest component is the power converter, which accounts for a further 12% of the mass. Tabulated mass breakdowns for both vehicles are given in Appendix H.

Figure 11 shows that the largest drag component is induced drag (drag due to lift): 43% and 53% of the total for the monoplane and box wing respectively. In addition, the monoplane cruise drag coefficient (1019 counts[††]) is almost twice that of the box wing (607 counts). This is not because the monoplane generates substantially more drag: monoplane cruise drag is 19.9 N, vs. 18.3 N for the box wing (Appendix I). Instead, the disparity exists because the box-wing planform area (0.772 m^2) includes the planform area of both the upper and lower wings; it is therefore much larger than the monoplane wing (0.492 m^2). Since the drag coefficient is referenced to the planform area, a higher planform area results in a lower drag coefficient.

While drag from the thruster nacelles is shown in Figure 11, drag from the thrusters is not. This is because thruster aerodynamic losses (from the electrodes and the inside of the duct walls) are modeled as a decrease in thrust, rather than as a contribution to drag. This is discussed further in Sections 2.4 and 2.6.

The optimizer generates converged solutions for both the monoplane and box wing, indicating that vehicles with the required capabilities can be designed and built. However, this result is contingent on the values of four key input parameters, which require further discussion:

- **Ionization energy E_{ion}:** the amount of electrical energy required to generate each ion.
- **Stage loss coefficient K_L:** pressure losses due to drag from 1 stage of thruster electrodes.
- **HVPC specific power p_{HVPC}:** output electrical power per unit mass of the high-voltage power converter.
- **Battery specific power p_{battery}:** output electrical power per unit mass of the battery.

Each of these parameters is discussed in detail in the following four sections.

3.2 Ionization energy

3.2.1 Sensitivity

As shown by Equation (15), the thruster electrical power draw is split into two components: ionization power and acceleration power. Ionization power is modeled via Equation (16); it is linearly related to E_{ion}, the amount of electrical energy required to generate an ion.

A sensitivity analysis was conducted with respect to ionization energy. Results are in Figure 12. Each point on the plot represents an optimized vehicle design; ionization energy is the only input parameter that is varied.

[††] Counts reference the drag coefficient, multiplied by 10^4; i.e., 1019 counts implies a drag coefficient of 0.1019.

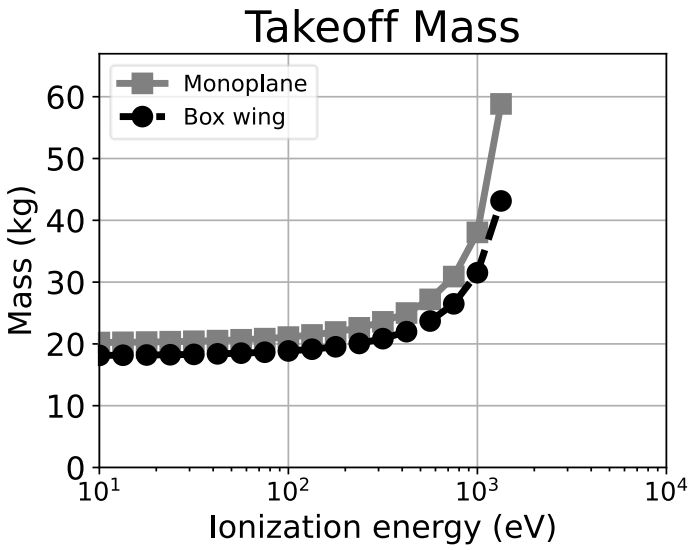

Figure 12: Vehicle takeoff mass vs. ionization energy.

3.2.2 Discussion

Figure 12 only shows data for $E_{\text{ion}} \lesssim 1{,}000$ eV. This is because the optimizer does not converge for ionization energies higher than this. Therefore, E_{ion} must be less than approximately 1,000 eV in order for the vehicles in this study to be feasible.

The default value of E_{ion} used in this study is 66 eV (see Table 4). This corresponds to the optimum energy required to generate an ion via electron impact in an electric field, and is known as Stoletov's constant [42]. This constant is discussed further in Section 4.1.6 of Ref. [43]. By contrast, experiments with EAD thrusters in which ionization energy was measured [17] yielded an energy of approximately 10,000 eV per ion generated, an order of magnitude greater than required here. These experiments are discussed further in Section 5.2.4 of Ref. [44].

3.2.3 Potential ion sources

It is clear from the preceding section that a significant reduction in E_{ion}, relative to existing EAD thruster technology, is required. In this section, ion sources with the potential to meet the E_{ion} requirement are discussed.

Table 11 shows the estimated ionization energy cost per ion for several ion sources, assuming that all the produced ions are extracted. Values are quoted as consumed by the onboard power source, so as to make them compatible with Equation (15). Each ion source is then discussed in detail in its respective section below.

Table 11: Estimated energy cost per ion for different ion sources. Power is assumed to be provided by the onboard power source.

Ion source	Ionization cost per ion/e^- pair (eV)
Electron-impact (optimum)	66
NRP discharge	350
Photoelectric effect	4.2[‡‡]
Photoionization	15.6[‡‡]
Radioactive decay	0[§§]

3.2.3.1 Nanosecond repetitively pulsed (NRP) discharges

Short, high-voltage pulses with high reduced electric field repeated at high frequency can result in ionization at a much lower energy cost per ion than DC or low-voltage AC discharges [42]. For this reason, nanosecond repetitively pulsed (NRP) discharges, with pulses with a duration of the order of nanoseconds and repetition frequencies of up to 1 MHz, offer the potential to consume low power in ionization. Macheret et al. [42] estimate that an NRP discharge with a 1 ns high-voltage pulse could result in an energy cost as low as 350 eV per ionization event in air at 1 atm and 2000 K.

Orrière et al. [45] recently tested an EAD device with an NRP discharge ion source and a flat plate collector. They achieved flow velocities of up to 2 m/s with a power draw 1 W. As they did not measure the DC current extracted by the flat plate, it is not possible to estimate the effective energy cost per extracted ion. Future work should test NRP discharges with different pulse duration, repetition frequencies, and peak voltages and measure the extracted current to estimate the ionization cost.

3.2.3.2 Photoelectric effect

When a photon of sufficiently high energy impacts a metallic surface, the surface may emit an electron due to the photoelectric effect. The surface's work function is the threshold for photoelectric electron emission and is a function of the surface's material: for example, the work function of aluminum is 4.2 eV [43], which means that photons with an energy of at least 4.2 eV (wavelength of at most 295 nm, in the UV spectrum) can result in photoelectric emission. In general, the more chemically reactive a metal is, the lower its work function.

The photoelectric effect has been proposed as a way to produce negative ions from air [46], and it could be used in EAD applications. In a potential implementation, electrons produced by the photoelectric effect would be accelerated from the emitter to a positively-biased collector by a DC electric field. The electric field distribution could be designed such that there is a high electric field

[‡‡] This value does not include efficiencies in light source and energy lost to heating, reflection and other processes.
[§§] Whereas ion generation from collisions between high-energy decay products and neutral molecules does consume energy from the decay products, there is no power consumption from the onboard power source.

region near the emitter, which results in the primary photo-electron causing an ionization cascade that produces secondary electrons and positive ions. These electrons would eventually attach to electronegative gas molecules, producing negative ions that would then drift toward the collector. The lowest possible energy cost per ion produced by the photoelectric effect is the surface's work function; however, the real energy cost is expected to be higher since some of the photons would be lost to heating and reflection.

Challenges with this ion source involve the UV light source design, which should be lightweight and efficient; and the electrode and light source design such that (i) photons strike as much of the emitter's surface as possible, and (ii) most of the intensity is transformed to photoelectric emission.

3.2.3.3 Photoionization

High-energy photons can be used to ionize gas molecules. For a photon to ionize a molecule, the photon energy must be higher than the molecule's ionization energy. The ionization energy of the nitrogen molecule is 15.6 eV [47], which corresponds to photons with a wavelength of 79.4 nm in the extreme UV range. A light source that could produce photons of this energy could ionize air efficiently; however, additional energy losses would be introduced by the UV light generation process.

The main challenge regarding photoionization is the generation of high-energy photons. It is possible to produce extreme UV light with solid-state sources via high harmonic generation. For example, patterning magnesium oxide crystals can produce photons of up to 20 eV by emitting the high harmonics of an 800 nm laser [48]. Alternative mechanisms may be needed for higher photon energies, such as vacuum tubes, but these introduce additional energy losses [49]. Another difficulty stems from the high photoionization cross-section of nitrogen, which results in low beam penetration distances, making air essentially opaque to extreme UV light [50]. Higher energy photons (into the X-ray spectrum) may be needed to reach practical penetration distances for volumetric ionization.

3.2.3.4 Radioactive decay

The radioactive decay of unstable nuclei could be used as the ion source in EAD devices, particularly in off-planet applications where safety is not a major concern. Out of the different decay mechanisms, alpha and beta (β^-) decays are probably the most promising options: alpha decay releases alpha particles (helium nuclei), and β^- decay releases high-energy electrons. In atmospheric-pressure air, alpha particles can only penetrate a few centimeters, whereas β^- particles can cover distances of the order of meters [51]. As alpha or β^- particles collide with neutral air molecules, ionization events take place, resulting in the production of secondary pairs of electrons and positive ions. Hence, a radioactive EAD emitter could produce either positive ions through ionization events, or negative ions following electron capture.

Americium-241 (which undergoes alpha decay) is used in household smoke detectors: the alpha particles produce ions and electrons from air in an ionization chamber, such that when a voltage is applied between two electrodes within the chamber, a current is produced. The presence of smoke alters the current. Therefore, by measuring the current, the smoke can be detected [52].

The main advantage of using radioactive ion sources in EAD systems is that they can provide ionization without drawing power from the onboard power supply; i.e., $E_{\text{ion}} = 0$. The criteria for the selection of radioactive ion sources for EAD systems would likely be similar to that used in radioisotope thermoelectric generators (RTGs) [53]. First, the material needs to have a half-life sufficiently long to perform a useful mission, but also short enough so that it has sufficient activity to produce the ions required by the EAD system. Second, the material needs to have a small rate of neutron and gamma-ray emissions, since these radiation types have high penetrating power and can damage electronics. Third, the decay products would ideally have to be stable, have a long half-life, or decay further without releasing significant gamma or neutron radiation.

3.2.4 Summary

It can be concluded from this section that methods of ion generation with ionization energies well below the value required by the vehicles in this study exist. Specifically, ions produced via NRP discharges, the photoelectric effect, photoionization, and radioactive decay all have ionization energies below 1,000 eV. Therefore, it may be possible to design an ion generation system incorporating one or more of these mechanisms into an EAD thruster. Further research into the design and fabrication of such a system is recommended as part of future work.

3.3 Stage loss coefficient

3.3.1 Sensitivity

As shown by Equation (4), the stage loss coefficient K_L represents pressure losses per thruster stage due to drag from the electrodes. K_L is the internal-flow system equivalent of the drag coefficient of an external-flow system.

A sensitivity analysis was conducted with respect to stage loss coefficient. Results are in Figure 13. Each point on the plot represents an optimized vehicle design; loss coefficient is the only input parameter that is varied.

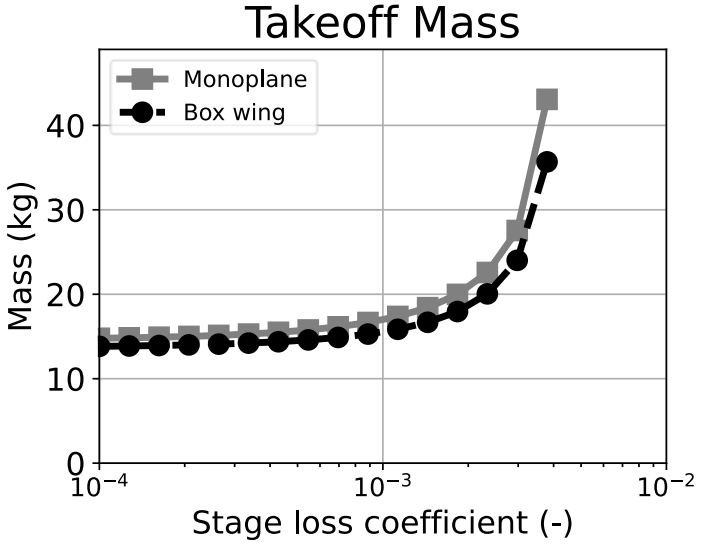

Figure 13: Vehicle takeoff mass vs. stage loss coefficient.

3.3.2 Discussion

Figure 13 only shows data for $K_L \lesssim 4.0 \times 10^{-3}$. This is because the optimizer does not converge for loss coefficients higher than this. Therefore, K_L must be less than approximately 4.0×10^{-3} in order for the vehicles in this study to be feasible.

Recall from Section 2.7.2 that the thruster electrodes consist of a grid of cylindrical wires. Table 7 shows that this geometry is directly used to compute the grid mass, by knowing the wire spacing, diameter, and material density. However, thruster losses are modeled via K_L, which is a fixed input parameter independent of geometry.

The loss coefficient can also be estimated based on the grid geometry output from the optimizer. Modeling approximations are as follows:

- The local flow velocity is equal to the thruster bulk velocity.
- The wires are cylindrical, so their drag can be estimated using cylinder drag coefficients.
- Each stage has 2 grids: the emitter grid and the collector grid.

Under these conditions, the stage loss coefficient can be estimated using

$$\mathrm{Re}_{\mathrm{wire}} = \frac{v_2 d_{\mathrm{wire}}}{\nu} \tag{28}$$

$$(C_d)_{\mathrm{wire}} = \left(2298.12\ \mathrm{Re}_{\mathrm{wire}}^{-0.958591} + 8.11799 \times 10^6\ \mathrm{Re}_{\mathrm{wire}}^{-3.80682}\right)^{\frac{1}{7.16293}} \tag{29}$$

$$D_{\mathrm{wire}} = \frac{1}{2}\rho v_2^2 l_{\mathrm{wire}} d_{\mathrm{wire}} (C_d)_{\mathrm{wire}} \tag{30}$$

$$(K_L)_{\mathrm{wire}} = \frac{D_{\mathrm{wire}}}{\frac{1}{2}\rho v_2^2 A_2} \tag{31}$$

where $\mathrm{Re}_{\mathrm{wire}}$ is the wire local Reynolds number, d_{wire} is the wire diameter, $(C_d)_{\mathrm{wire}}$ is the wire drag coefficient, l_{wire} is the emitter + collector wire length (estimated using the grid geometry discussed in Section 2.7.2), D_{wire} is the wire drag, and $(K_L)_{\mathrm{wire}}$ is the wire loss coefficient. Equation (29) was obtained using a posynomial fit [54] to cylinder drag data from Figure 1.12 of Ref. [55]. Data was obtained for $1 \leq \mathrm{Re}_{\mathrm{wire}} \leq 1{,}000$; the fit RMS error was 3.6%.

This model was applied to the thrusters on both aircraft, across all four mission segments with distinct thruster data (hover, cruise, climb, and bank). Results are in Table 12.

Table 12: Stage loss coefficients, estimated using Equations (28)-(31).

		Stage loss coefficient			
Aircraft	**Thruster**	**Hover**	**Cruise**	**Climb**	**Bank**
Monoplane	Box-tail thruster	0.15	0.14	0.14	0.14
	Forward thrusters	0.15	0.14	0.14	0.14
Box wing	Box-tail thruster	0.15	0.14	0.14	0.15
	Box-wing thruster	0.15	0.14	0.14	0.15

Table 12 shows that the stage loss coefficients range from 0.14-0.15, about 70-75 times higher than the loss-coefficient value of 2.0×10^{-3} used by default by the optimizer (Table 4). Moreover, Figure 13 shows that the optimizer does not converge with loss coefficients this high. A substantial reduction is needed for the vehicles in this study to be feasible.

The following geometric means of reducing the loss coefficient are investigated:

- **Using vertical wires only,** eliminating the horizontal wires. The wire length (and by extension, the loss coefficient) is thus reduced by a factor of 2. The resulting electric field is still approximately one-dimensional, consistent with the thruster modeling approximations in Section 2.4.
- **Increasing the wire spacing** from 25% to 100% of the gap spacing. This reduces the loss coefficient (again via wire length) by a factor of 4. This spacing has been used in MSD thruster has experiments conducted by the authors (Appendix B).
- **Reducing the wire diameter.** The default value of 56 microns is based on MSD thruster experiments conducted by the authors (Appendix B), but tungsten wires as small as 7.6 microns in diameter can be obtained commercially [56].
- **Using streamlined electrode units,** each or which contains an emitter, collector, and ion source. This is shown in Figure 14.

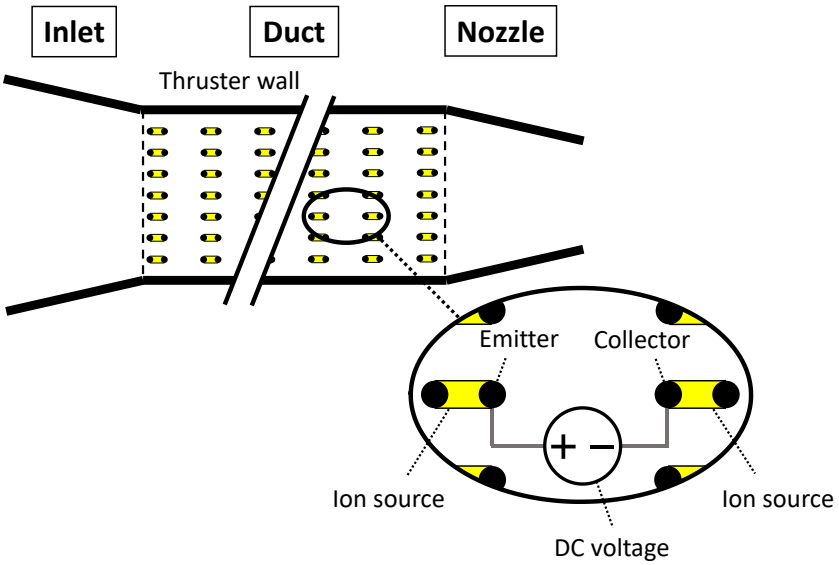

Figure 14: Side view of an MSD thruster with streamlined electrode units (inset), each of which contains an emitter, collector, ion source (yellow), and applied DC voltage source.

The first three listed means of reducing the loss coefficient can be modeled via Equations (28)-(31), simply by changing the wire length and diameter. However, Figure 14 shows that each streamlined electrode unit is roughly shaped like an ellipsoid. Estimates for ellipsoid drag at such low Reynolds numbers (about 10-20) could not be obtained. Instead, the drag of the streamlined electrode unit is approximated as that of a cylinder, with the same diameter as the collector wires. This effectively eliminates the emitter drag, reducing the loss coefficient by a factor of 2.

These geometric loss-coefficient reduction techniques are applied successively to each thruster. Results are in Figure 15 and Figure 16 for the monoplane and box wing respectively. Note that the *y*-axis is logarithmic.

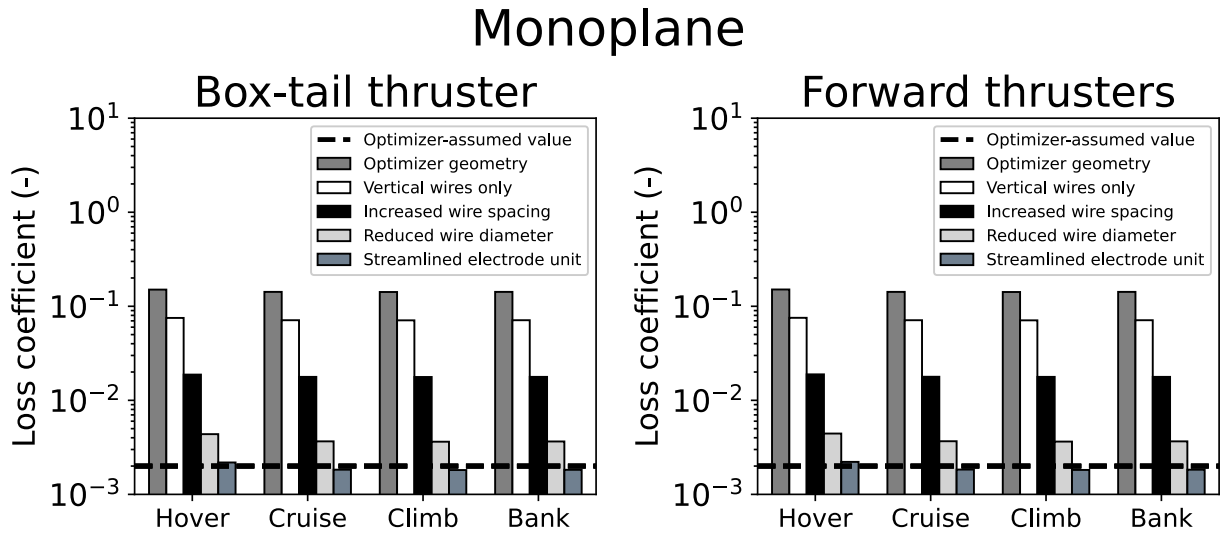

Figure 15: Thruster stage loss coefficient as a function of grid geometry model for the monoplane.

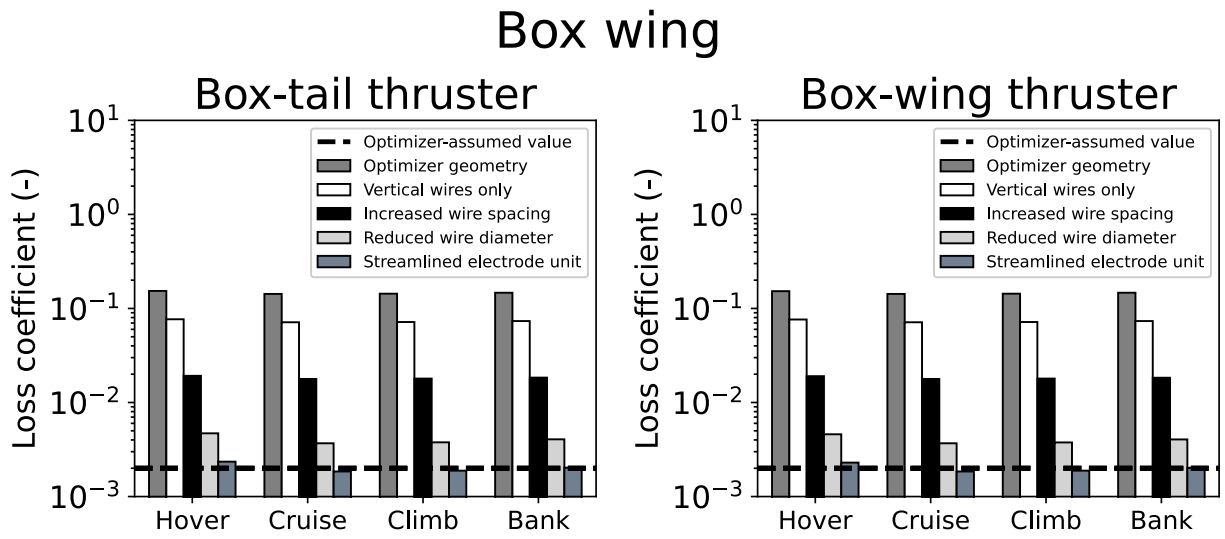

Figure 16: Thruster stage loss coefficient as a function of grid geometry model for the box wing.

Figure 15 and Figure 16 show that the loss coefficient decreases as each successive geometry modification is applied. If all four changes are applied at once (the "streamlined electrode unit" bars), the loss coefficient is approximately equal to the optimizer default value of 2.0×10^{-3} (the black dotted lines). Therefore, it may be possible to obtain a stage loss coefficient low enough to

enable the vehicles in this study. However, these grid geometries have yet to be demonstrated experimentally.

3.3.3 Microfabrication

Small-scale manufacturing techniques may enable the manufacturing of very thin wires or arrangements, such as those in Figure 14. Wires with small diameters can be manufactured from metal stock by subjecting the metal to several sequential drawing processes, with each process resulting in a lower-diameter wire [57]. Tungsten wires with a diameter as small as 7.6 microns are commercially available [56]; even smaller wires could be manufactured using similar techniques. Micro-extrusion, in which metal or polymer stock is pushed through a die, could be used to manufacture electrodes of any arbitrary shape, including airfoils. Features of the order of 10 microns have been demonstrated through extrusion [57].

For more complex geometries, such as monolithic (built in a single piece) grids of electrodes, techniques such as injection molding could be employed. Microcasting, in particular, is expected to be a suitable candidate for this purpose. Microcasting involves producing a 3-D mold for the desired piece and then filling it with molten metal. Additional processes, such as applying centrifugal forces, are needed to ensure that the metal is evenly distributed within the mold [57].

To reduce mass, it may be advantageous to apply a metallic coating to a polymer core instead of having the entire feature made of the same metal. While manually applying the metallic coating (e.g., aluminum tape) is possible, there are manufacturing techniques that could improve surface finish. Electroplating is a surface treatment process in which ions of some species dissolved in a fluid are deposited on the surface of an electrically-conductive material when a potential difference is applied between two electrodes [58]. Even though polymers are not conductive, they can still be electroplated. However, an additional preparation step is needed, wherein a first metallic layer is deposited on the polymer to make it conductive.

Sputter deposition is an alternative process, in which the material to be coated does not need to be conductive. In sputtering deposition, ions are shot toward a target, causing ejection of ions in the target by sputtering. The target ions then reach the substrate that is to be coated and deposit on its surface [58]. Either of these techniques could be employed to produce the streamlined electrode unit in Figure 14. For example, the ion source in the middle of the unit could be made from non-conductive material; afterward, targeted electroplating could be used to ensure that the leading and trailing edges are conductive.

3.3.4 Summary

It can be concluded from this section that the default thruster electrode geometry (Section 2.7.2) results in stage loss coefficients too high for the vehicles in this study to be feasible. However, reductions in loss coefficient sufficient to render the vehicles feasible can be obtained by modifying the geometry, and micromanufacturing techniques can be used to build the resulting advanced electrode geometries. These advanced geometries have yet to be demonstrated experimentally, although they appear feasible at this stage.

3.4 Power-converter specific power

3.4.1 Sensitivity

As discussed in Section 2.5, the power-converter specific power p_{HVPC} is equal to the maximum available output power of the power converter divided by its mass.

A sensitivity analysis with respect to power-converter specific power is shown in Figure 17. Each point on the plot represents an optimized vehicle design; power-converter specific power is the only input parameter that is varied.

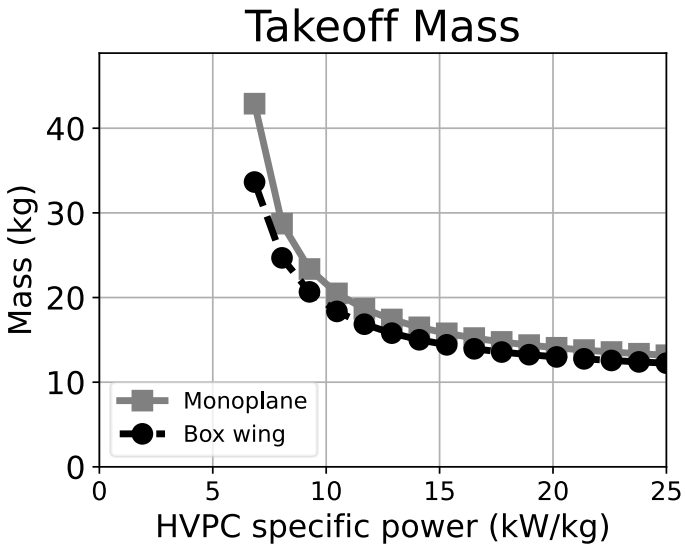

Figure 17: Vehicle takeoff mass vs. power-converter specific power.

3.4.2 Discussion

Figure 17 only shows data for $p_{\mathrm{HVPC}} \gtrsim 7$ kW/kg. This is because the optimizer does not converge for specific power values lower than this. Therefore, p_{HVPC} must be less than approximately 7 kW/kg in order for the vehicles in this study to be feasible. By contrast, the V2 power converter (see Section 1.2) had a specific power of approximately 1.03 kW/kg[***]. The default specific power in this study (10.3 kW/kg) is ten times higher.

The functional dependence of power-converter mass can be stated as

$$m_{\mathrm{HVPC}} = f(V_{\mathrm{in}}, V_{\mathrm{out}}, P_{\mathrm{out}}, \dots) \tag{32}$$

i.e., the power-converter mass m_{HVPC} is a function of input voltage V_{in}, output voltage V_{out}, and output power P_{out}, among other variables. Power-converter mass can be reduced by increasing the input voltage, lowering the output voltage, or reducing the output power.

[***] Ref. [16] gives a power-converter mass and input power of 0.51 kg and 620 W respectively, while the efficiency ranges from 82-85%. Since the power converter is most efficient at its upper power limit [19], the higher efficiency value (85%) is used to estimate the output power as 527 W, yielding a specific power of 1.03 kW/kg.

Equation (32) can be used to frame a series of arguments, explaining why a significant increase in p_{HVPC} (relative to the V2 aircraft flown by Xu et al. [16]) may be achievable for the vehicles in this study. They are as follows:

- **Higher input voltage,** due to a larger battery. The V2 battery had a mass of 0.23 kg [16], while the vehicles in this study have battery masses of 6-8 kg (Appendix H), more than 25 times greater. Since battery pack voltage can be increased by wiring cells together in series, the pack voltages (V_{in}) of the vehicles in this study can be higher than that of the V2, reducing HVPC mass.
- **Lower output voltage,** due to multistaging. This was mentioned in Section 1.2 as one of the advantages of MSD thrusters, relative to their exposed counterparts: multiple miniaturized thruster stages allow for a lower power-converter output voltage. The V2 thrusters required a voltage of 40 kV [16], while the thrusters in this study use a maximum voltage of only 10 kV (Table 4), which will lead to mass reductions.
- **Higher output power.** Power-converter specific power roughly scales with $P_{\mathrm{out}}^{0.25}$ [19]. The V2 power-converter maximum output power is approximately 527 W (see above footnote[***]), while those of the monoplane and box wing are more than 40 times greater: 25.4 kW and 22.8 kW respectively (Table 20 and Table 21). If the scaling law holds, this effect alone should increase specific power of both vehicles by a factor of approximately 2.6.
- **Continuous vs. burst power.** Many power-electronic devices have burst power limits that are higher than their continuous-power limits; i.e., they can be operated above their continuous-power limit for short periods of time. For example, Teplechuk et al. designed and built an amplifier (which serves a similar purpose to a power converter) with a burst output power more than twice the continuous output power [59]. Meanwhile, the aforementioned maximum power estimates for the monoplane and box wing only apply in hover, which lasts 20 seconds or less[†††]. By contrast, Table 20 and Table 21 show that the cruise power is 4.75 kW for the monoplane (5.3 times lower than in hover) and 4.23 kW (5.4 times lower than in hover) for the box wing. Therefore, it may be possible to size the power-converters to the continuous (cruise) power requirement, rather than the peak (hover) power requirement. This should allow for further mass reductions.

It can be concluded from this section that a substantial increase in p_{HVPC}, relative to that of the V2 aircraft, is required in order for the vehicles in this study to be feasible. Significant improvements should be possible: given the above arguments, an order-of-magnitude opportunity space is available. However, detailed power-converter design and experimental validation is required for confirmation. This is recommended as part of future work.

[†††] Table 2 states that the takeoff, payload-drop, and landing hover times are 5 s, 20 s, and 5 s respectively.

3.5 Battery specific power

3.5.1 Sensitivity

As discussed in Section 2.5, the battery specific power p_{battery} is equal to the maximum available output power of the battery, divided by its mass.

A sensitivity analysis with respect to battery specific power is shown in Figure 18. Each point on the plot represents an optimized vehicle design; battery specific power is the only input parameter that is varied.

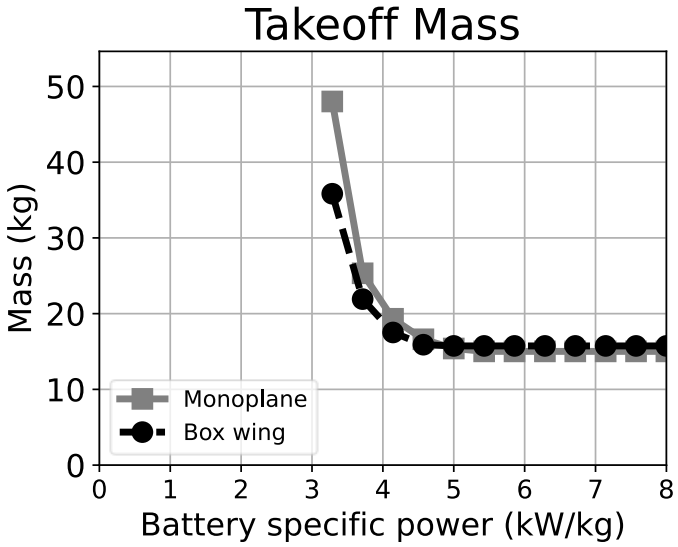

Figure 18: Vehicle takeoff mass vs. battery specific power.

3.5.2 Discussion

Figure 18 only shows data for $p_{\text{battery}} \gtrsim 3$ kW/kg. This is because the optimizer does not converge for specific power values lower than this. Therefore, p_{battery} must be greater than approximately 3 kW/kg in order for the vehicles in this study to be feasible.

Recall from Section 2.5 that the battery is sized by three parameters: specific energy, specific power, and density. Figure 18 shows that vehicle mass is independent of battery specific power above 5 kW/kg. Therefore, the specific power constraint becomes inactive above this point; the battery is only sized by specific energy and density.

The default value of battery specific power in this study is 4 kW/kg (Table 5), about twice that of existing lithium-ion battery prototypes [39]. However, the specific power of lithium-polymer batteries in the literature can be as high as 3 kW/kg [60]. In addition, batteries can have burst (pulse) current limits that are higher than their continuous-current limits. The upper current limit is typically dependent on the battery module geometry. For example, a commercially available battery module [61] has a maximum pulse discharge current more than twice as high as its continuous discharge current. It was shown in Section 3.4.2 that the continuous (cruise) power requirements for the aircraft in this study are more than five times lower than the peak (hover)

requirements. Therefore, it may be possible to design a battery pack with the required specific power using existing technology.

4 Conclusions

In this work, two uncrewed aircraft (a monoplane and a box wing) were designed and optimized for an urban package delivery mission. The aircraft are powered by MSD thrusters, and are capable of VTOL. Unlike propeller-driven aircraft, they have no moving parts in their propulsion system (except for the components that enable the thrusters to tilt). They may therefore be able to complete urban package delivery missions without community opposition to noise.

An efficient multidisciplinary optimization framework, utilizing signomial programming, was developed to design and optimize the vehicles. The framework incorporates a one-dimensional physics-based model for MSD thrusters, along with aerodynamic, structural, weight, and power-electronics models. The framework was used to generate designs for both aircraft, including dimensions, mass breakdowns, and performance data. It was also used to conduct sensitivity analyses.

Requirements for an out-and-back urban package delivery mission were defined, based on package delivery services under development. Both MSD aircraft are capable of flying the nominal mission. However, this is contingent on advances in four key technologies relative to today's state of the art. The identification of these technologies, as well as the associated parameter by which improvement can be quantified, is a key contribution of this work. The technologies and parameters are as follows:

- **More-efficient ion generation methods** with reduced power draw, quantified via the ionization energy E_{ion}.
- **Miniaturized thruster electrodes** with lower duct pressure losses, quantified via the stage loss coefficient K_L.
- **Lighter power converters** with greater output power, quantified via the power-converter specific power p_{HVPC}.
- **Lighter batteries** with greater output power, quantified via the battery specific power p_{battery}.

Future work should focus on characterizing and improving these technologies.

Appendix A EAD acoustic measurements

In order to estimate the noise reductions achievable with EAD thrusters, the authors conducted a preliminary experiment to measure the sound of an EAD thruster and a propeller. Power spectral density vs. sound frequency for both systems is shown in Figure 19. The experiment was conducted under static conditions (i.e., zero freestream velocity), and a thrust of 0.7 N. The EAD thruster was an exposed (i.e., no duct) wire-to-airfoil thruster with a span of 2.9 m, a gap spacing of 120 mm, and a voltage of 70 kV. A two-bladed 8040 (8in diameter; 4in pitch) propeller, powered by a brushless motor, was used for comparison.

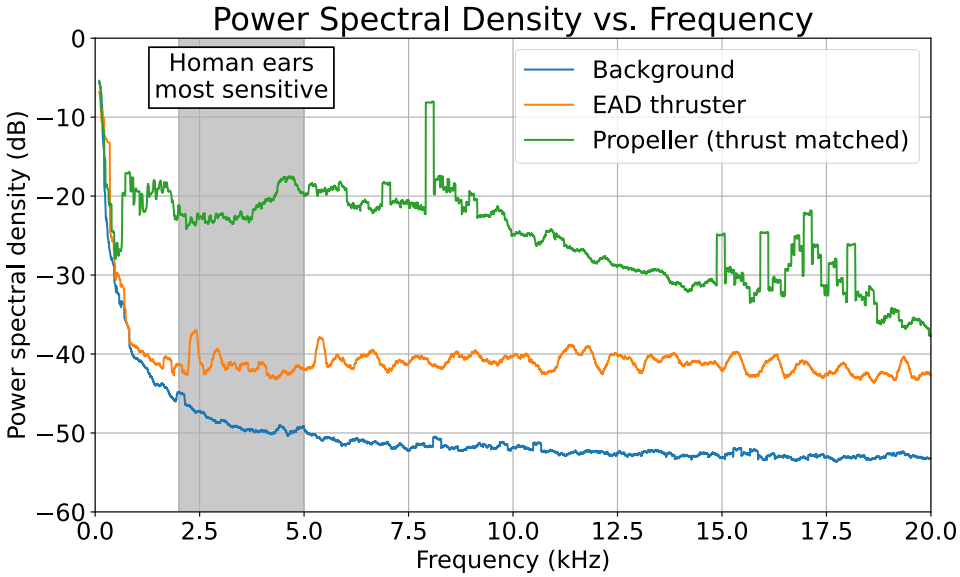

Figure 19: Power spectral density vs. frequency for an EAD thruster and a propeller.

Figure 19 shows that the EAD thruster is much quieter than the propeller, especially around 2.5-5 kHz, the frequency region where human ears are most sensitive [62], [63]. By integrating the data in Figure 19, it can be shown that the EAD thruster is approximately 20 dB quieter than the propeller at the same thrust. This is equivalent to a noise reduction of 99%, or two orders of magnitude[‡‡‡].

Note that Figure 19 shows power spectral density (rather than sound pressure level). This allows for a comparison between the propeller and the EAD thruster, but the sound pressure level itself was not determined.

[‡‡‡] The mean square sound pressure is the metric that has been reduced by 99%. Mean square sound pressure P_{RMS}^2 (measured in Pascals squared) is related to the sound pressure level SPL (measured in decibels) as follows: $\mathrm{SPL} = 10\log_{10}(P_{\mathrm{RMS}}^2/P_{\mathrm{ref}}^2)$. $P_{\mathrm{ref}} = 2\times10^{-5}$ Pa is the reference pressure. This equation can be manipulated to show that a 90% reduction in P_{RMS}^2 (one order of magnitude) corresponds to an SPL reduction of 10 dB; a 99% reduction in P_{RMS}^2 (two orders of magnitude) corresponds to an SPL reduction of 20 dB.

Appendix B Ducted thruster experiments

Experiments were performed on a single-stage ducted thruster to validate some of the predictions from the simple momentum theory in Gomez-Vega et al. [20], which serve as the basis of the models used in this study. Figure 20 shows the setup used in these experiments. The thruster contained parallel pairs of 56-micron-diameter tungsten wire emitters and flat-plate aluminum-covered collectors with a 25.4 mm chord and a thickness of 1.1 mm. The internal cross-section was rectangular, 600 mm by 400 mm, and contained 20 emitter/collector pairs, separated from each other by a distance of 20 mm. The gap spacing, d, separating the emitters from the leading edge of the collectors was 20 mm. The duct was made from blue foam and consisted of a parabolic inlet with a length of 80 mm in the longitudinal direction and a width of 35 mm in the transverse direction, a straight portion with a length of 40 mm where the electrodes were placed, and a straight nozzle with a divergent angle of 20°. The duct had a thickness of 15 mm, and the external portion of the nozzle was straight, forming an angle of 10° with the longitudinal axis (see Figure 20c for duct coordinates). To ensure electrical continuity, the emitters were connected to two 3D-printed electrode holders covered in copper tape, and the collectors were connected to each other via thin insulated wires flushed against the side of the thruster.

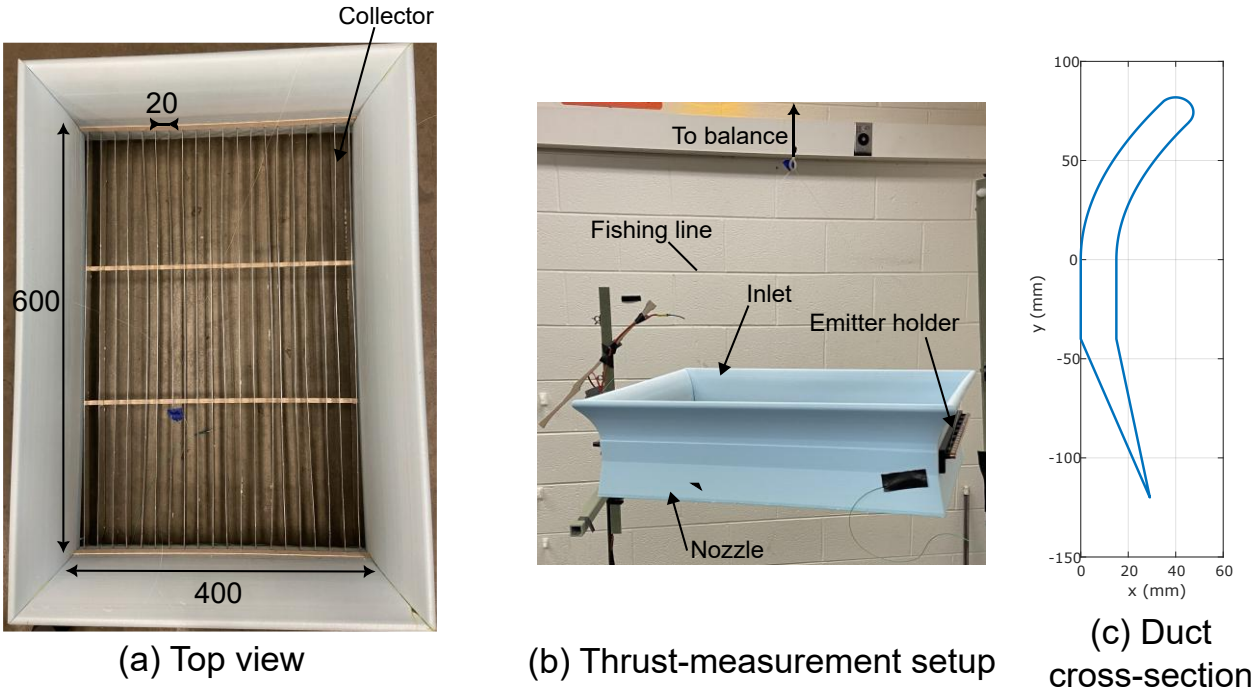

Figure 20: Single-stage ducted thruster used to validate theoretical predictions. In (a), a top view of the thruster is shown; (b) shows the thruster suspended from the balance by fishing lines; (c) shows the cross-section of the duct, with the inlet and nozzle profiles. Dimensions in mm.

The thruster was suspended from a Sartorius Entris 4202 balance by fishing line; the static thrust force was estimated as the change in weight when the thruster was on. Ions were generated using a DC corona discharge; a Matsusada Precision AU-50P12 positive power supply was used to produce the corona discharges. Two types of tests were performed: positive-corona experiments,

in which the emitters were connected to the output of the positive supply and the collectors were grounded; and negative-corona tests, in which the emitters were grounded and the collectors were connected to the positive supply. Current and voltage measurements were provided automatically by the power supply.

The static thrust–voltage characteristics of this ducted thruster are shown in Figure 21a, where tests were done up to the maximum voltage before sparking in steps of 1 kV. The results show that a thruster with a positive corona can produce a maximum thrust of up to 1.13 N, corresponding to a thrust density (thrust per unit area) of 4.71 N/m^2 per stage and a thrust-to-power ratio of 7.9 N/kW. Figure 21b shows how the thrust-to-power ratio changes with the thrust density for the two corona polarities. As a reference, the two-stage thruster used to produce the first EAD-propelled aircraft, described in Xu et al. [16], produced a net thrust of approximately 3.2 N, with a thrust density of 3.6 N/m^2 and a thrust-to-power ratio of 6.2 N/kW. The results show that this single-stage thruster can produce a thrust of the same order of magnitude as the two-stage thruster in Xu et al. [16], with higher thrust density and thrust-to-power ratio.

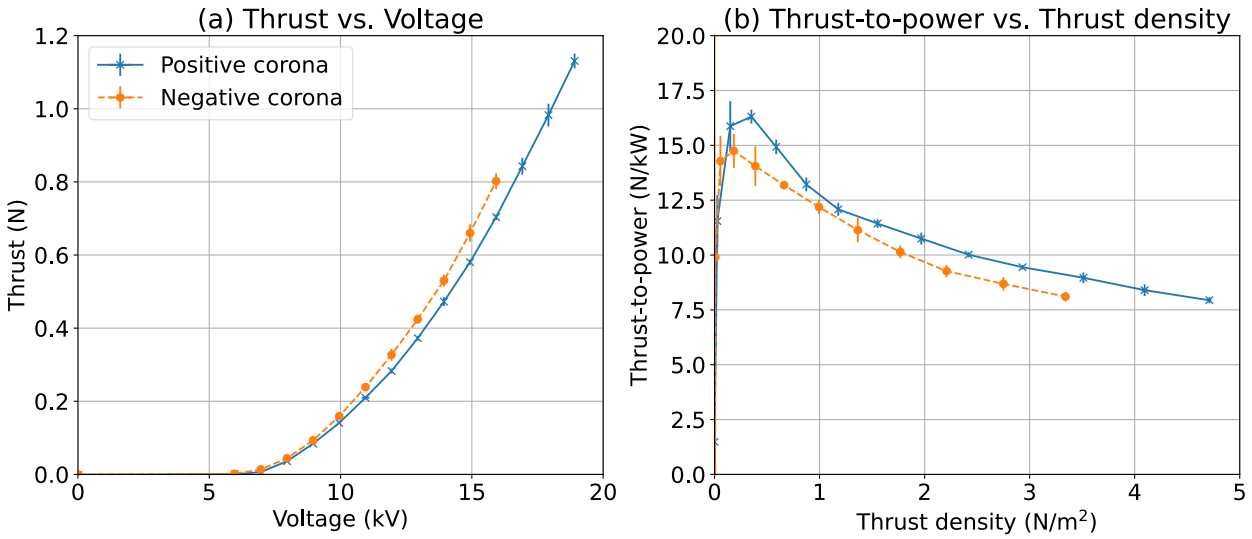

Figure 21: (a) Thrust against voltage and (b) thrust-to-power ratio against thrust density produced by the ducted thruster with either positive or negative coronas.

In an unducted thruster with negligible drag forces, the thrust force is equal to the integral of the Coulomb body force in the gap and is given by [15]

$$T = \frac{Id}{\mu},$$

where I is the current drifting between the electrodes. Therefore, a plot of the thrust produced by an unducted thruster versus the product of current and gap spacing should be a straight line with a slope of $1/\mu$. This relationship between thrust and current is not expected to hold when the thruster has a duct, due to the thrust component from the pressure forces acting on the duct.

Figure 22 shows the thrust per unit electrode span, b_e, versus the product of current per unit span and gap spacing obtained with the ducted thruster tested here. A shadowed band showing the unducted thrust for the range of ion mobilities reported in the literature ($1.8 \times 10^{-4} \leq \mu \leq 2.5 \times 10^{-4}$ m^2 V^{-1} s^{-1}) is also shown [64], along with a line corresponding to the mobility used in this study. The results show that the ducted thruster with either positive or negative coronas produces significantly more thrust for a given current than what would be predicted if the thruster were unducted. This is compatible with the predictions from momentum theory, in which ducted thrusters produce more thrust than their geometrically-similar unducted counterparts.

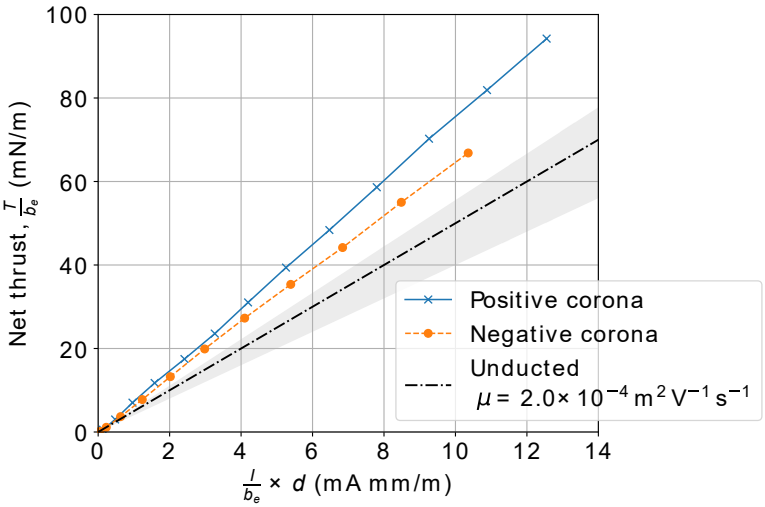

Figure 22: Thrust per unit span against product of current per unit span and gap spacing. EAD theory predicts the relationship between the variables to be linear and to lie within the shaded region (range of ion mobilities in the literature) if the thruster is unducted.

Appendix C Vehicle 3-view sketches

3-view sketches of the monoplane are shown in Figure 23 – Figure 28; 3-view sketches of the box wing are shown in Figure 29 – Figure 34. All sketches are drawn using dimensions from the design optimization results; they are therefore to scale.

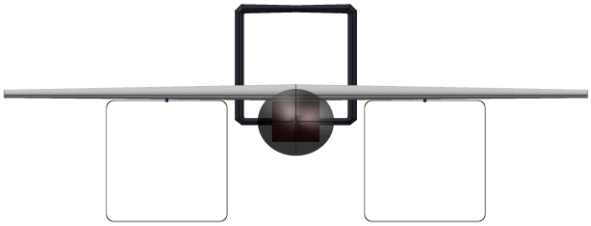

Figure 23: Front view of the monoplane in wingborne flight.

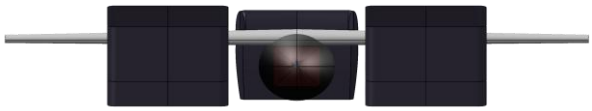

Figure 24: Front view of the monoplane in hover.

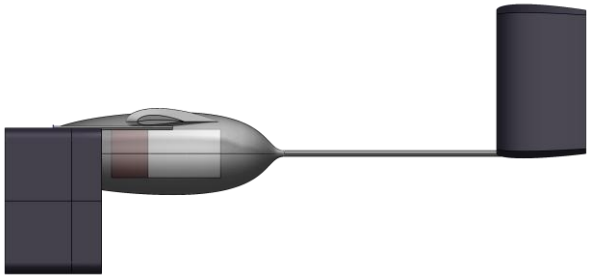

Figure 25: Side view of the monoplane in wingborne flight.

Figure 26: Side view of the monoplane in hover.

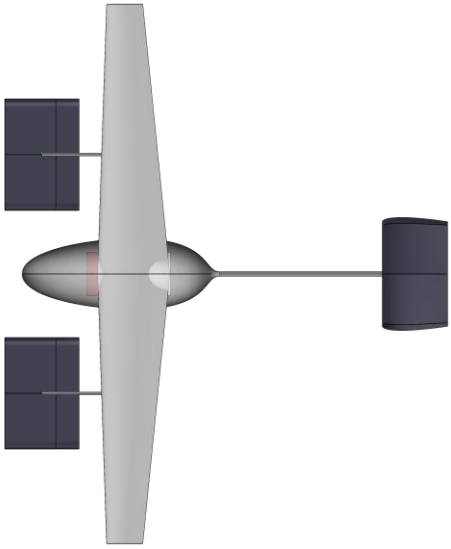

Figure 27: Top view of the monoplane in wingborne flight.

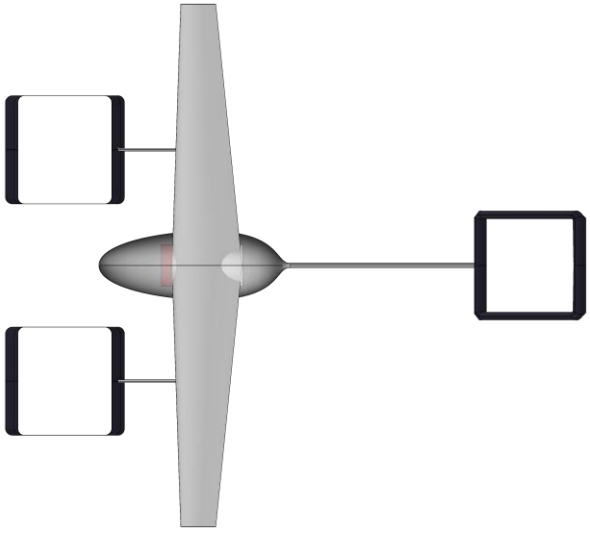

Figure 28: Top view of the monoplane in hover.

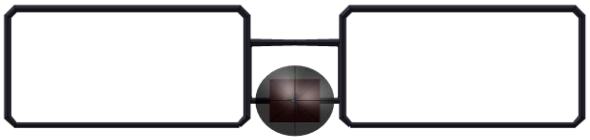

Figure 29: Front view of the box wing in wingborne flight.

Figure 30: Front view of the box wing in hover.

Figure 31: Side view of the box wing in wingborne flight.

Figure 32: Side view of the box wing in hover.

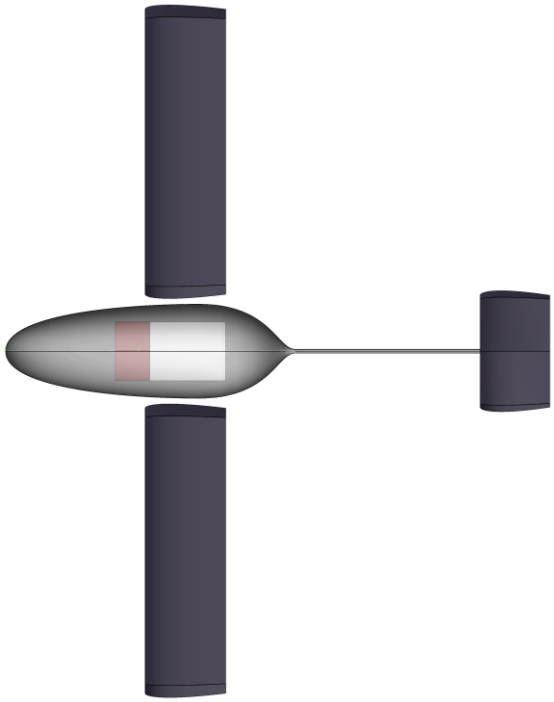

Figure 33: Top view of the box wing in wingborne flight.

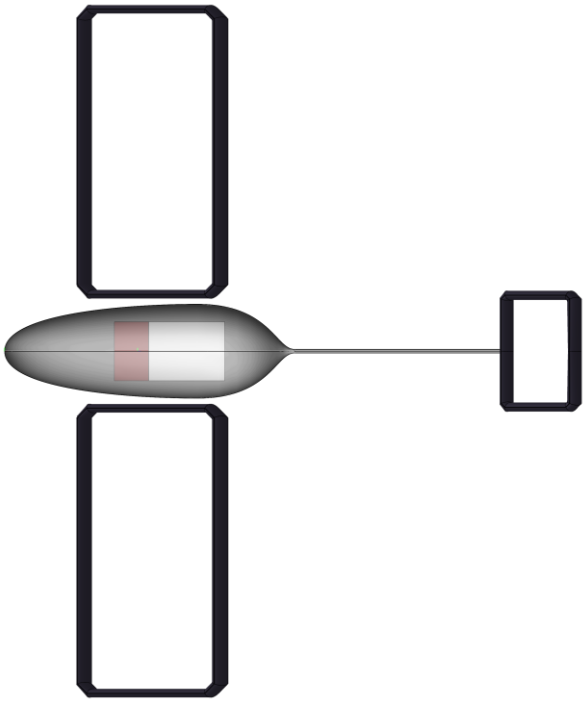

Figure 34: Top view of the box wing in hover.

Appendix D Thruster model modifications

As mentioned in Section 2.4, equations (2), (3), (5), (9), (11), and (15) are solved in a different form. This is done for one of two reasons:

- **The original form is not SP-compatible.** As mentioned in Section 2.3, a signomial program (the design optimization algorithm used in this work) requires that all models be formulated as monomial, posynomial, and signomial functions.
- **The original form is an equality, when an inequality would suffice.** In a signomial program, inequality constraints are generally more numerically efficient and robust than equality constraints. Posynomial equality relaxation [27] ensures that all inequality constraints are exactly satisfied at the optimum.

Therefore, for design optimization, equations (2), (3), (5), (9), (11), and (15) are written as equations (33)-(38) respectively:

$$v_4^2 \leq v_\infty^2 + 2\frac{\Delta P}{\rho} \tag{33}$$

$$\frac{T}{A_2} + \frac{D_{\text{wall}}}{A_2} + \rho v_4 v_\infty \phi \leq \rho v_4^2 \phi \tag{34}$$

$$n(\Delta P)_{\text{EAD}} \geq \Delta P + n(\Delta P)_{\text{loss}} \tag{35}$$

$$\overline{(\Delta P)_{\text{EAD}}} + \frac{1}{3}\overline{v_2}^2 \leq 1 + \frac{2}{3}\overline{v_2} \tag{36}$$

$$\bar{j} \geq 1 + 2\overline{v_2} + \overline{v_2}^2 \tag{37}$$

$$\frac{P}{A_2} \geq \left(\frac{P}{A_2}\right)_{\text{ion}} + \left(\frac{P}{A_2}\right)_{\text{accel}} \tag{38}$$

Appendix E Box wing modeling details

Modeling details specific to the box wing are discussed in this Appendix.

Lift distribution: unlike for a monoplane, the optimal lift distribution of a box wing is not elliptical [65], [66]. Instead, it consists of "a constant and an elliptical part for the horizontal wings and a linear and butterfly-shaped part for the vertical wings" [65]. This should in principle affect the box-wing drag and structural models, but it is neglected for the purpose of this study. Instead, a conservative value of wing span efficiency (Table 6) is used.

Induced drag: like all nonplanar wing configurations, induced drag of the box wing is affected by interference between the two wings. This can be expressed as a function of the wing height-to-span ratio [65], [67] as

$$\frac{(D_i)_{\text{box}}}{(D_i)_{\text{planar}}} = f\left(\frac{h}{b}\right) = \frac{k_1 + k_2\frac{h}{b}}{k_3 + k_4\frac{h}{b}} \tag{39}$$

where D_i is induced drag, h is the wing height (vertical distance between the upper and lower wings), b is the wingspan, and k_1-k_4 are constants. The subscripts $(\ \ )_{\text{box}}$ and $(\ \ )_{\text{planar}}$ refer to the box wing and to an equivalent planar wing respectively.

Box wing height is an optimizer design variable, but Equation (39) is not used directly in design optimization. This is because Equation (39) is a signomial equation, which cannot generally be solved as efficiently as a monomial or posynomial [32]. Instead, values for k_1-k_4 were obtained from Ref. [57]. A posynomial fit [54] to Equation (39) was then obtained as

$$\frac{(D_i)_{\text{box}}}{(D_i)_{\text{planar}}} = \left[0.941763\left(\frac{h}{b}\right)^{-0.0195267}\right]^{10} \tag{40}$$

Equation (40) corresponds to data for $0.03 \leq \frac{h}{b} \leq 0.8$; the fit RMS error was 3.99%. Equation (40) is a monomial, and was directly implemented in design optimization.

Wing curvature: the wing structural model (Table 7) assumes the wing bends with constant curvature due to the applied lift force. Ref. [41] shows that this approximation is reasonable for a wing taper ratio of 0.5 (the monoplane value), but overestimates the wing tip deflection for a taper ratio of 1.0 (the box wing value). Since the wing tip deflection is constrained to below 5% of the wingspan for both vehicles, constant bending curvature is therefore a conservative approximation.

Electroaerodynamic interference: the box wing contains a thruster, so the lift and induced drag of the wing should be affected by the thruster, and vice versa. For the purpose of this study, this effect is neglected. Instead, it is assumed that lift and induced drag are both independent of thrust. The same approximation is made for the box tail.

Appendix F Hover balance model

Both vehicles must balance in hover; i.e., the sum of the moments from each thruster, taken about the vehicle center of gravity (CG), must sum to zero. Models for ensuring this are the subject of this Appendix.

For the purpose of design optimization, the center of gravity of both vehicles is assumed to be located 60% of the distance along the fuselage-pod length, and also at the wing 50% chord position. Ideally, the payload centroid should also be on the CG, so that it does not shift if the payload is changed or dropped.

A side view of the monoplane in hover, including the hover balance model parameters, is shown in Figure 35.

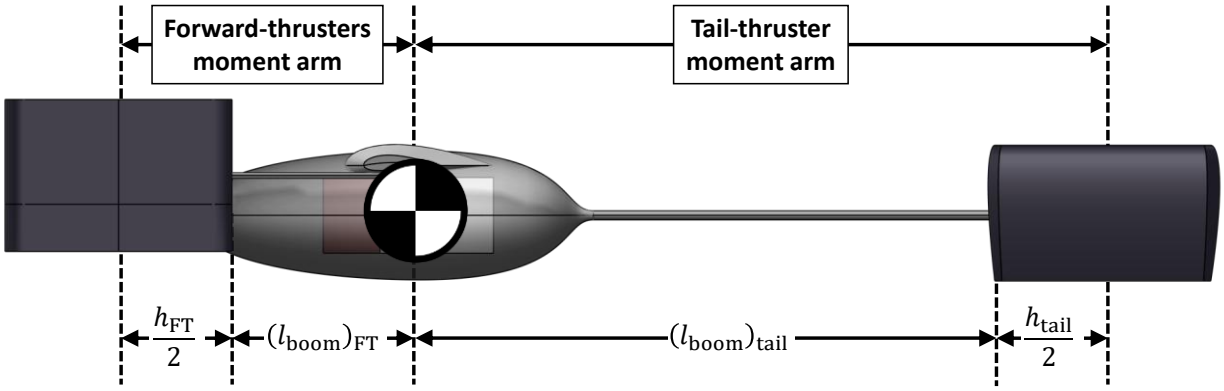

Figure 35: A side view of the monoplane, showing the hover balance model parameters.

The forward-thruster booms extend forwards from the CG to the forward thrusters, while the tail boom extends backwards from the CG to the box tail. Therefore, the moment arms of the forward thrusters and tail thruster are computed as

$$(l_{\text{momentArm}})_{\text{FT}} = \frac{h_{\text{FT}}}{2} + (l_{\text{boom}})_{\text{FT}} \tag{41}$$

and

$$(l_{\text{momentArm}})_{\text{tail}} = \frac{h_{\text{tail}}}{2} + (l_{\text{boom}})_{\text{tail}} \tag{42}$$

respectively, where $l_{\text{momentArm}}$ is the moment-arm length and h is the height. The subscripts $(\ \ )_{\text{FT}}$, $(\ \ )_{\text{boom}}$, and $(\ \ )_{\text{tail}}$ refer to the forward thrusters, boom, and tail respectively.

Because the CG is located at the wing 50% chord position, the forward-thruster boom must be at least as long as half the wing root chord. The forward thrusters are also offset forwards from the wing by an amount equal to half the forward-thruster height, to ensure that their flow fields do not interfere in hover. This can be stated mathematically as

$$(l_{\text{boom}})_{\text{FT}} \geq \frac{1}{2} h_{\text{FT}} + \frac{1}{2} (c_{\text{root}})_{\text{wing}} \tag{43}$$

where $(c_{\text{root}})_{\text{wing}}$ is the wing root chord.

Finally, the hover balance constraint can be written as

$$2(T_{\text{hover}})_{\text{FT}} (l_{\text{momentArm}})_{\text{FT}} = (T_{\text{hover}})_{\text{tail}} (l_{\text{momentArm}})_{\text{tail}} \tag{44}$$

where T_{hover} is the hover thrust. The factor of 2 accounts for the 2 forward thrusters.

A side view of the box wing, including the hover balance moment arms, is shown in Figure 36.

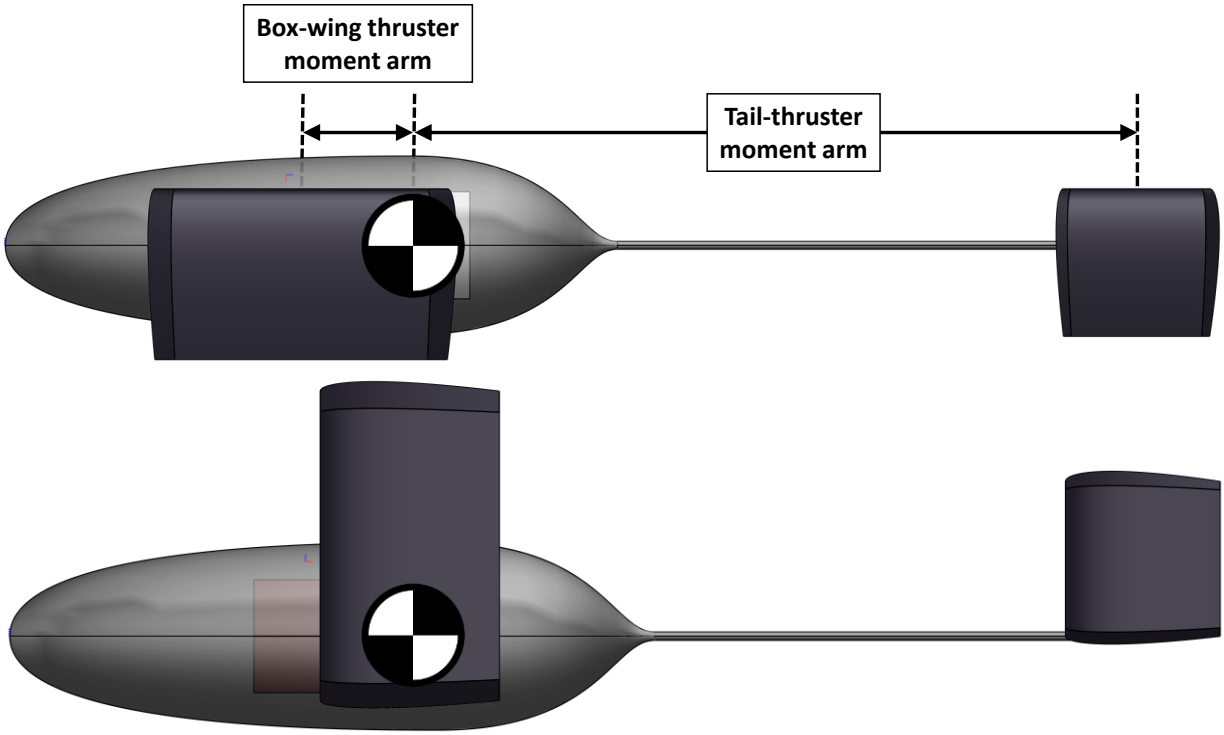

Figure 36: a side view of the box wing, in hover (top) and in wingborne flight (bottom).

Equations (41)-(44) are required for the monoplane, to set the length (and, by extension, the mass and drag) of the forward-thruster booms during optimization. The box wing lacks a similar set of optimization constraints. Instead, the box-wing thruster pivot location (relative to the fuselage) is selected during post-processing, to ensure that the vehicle balances in hover. Figure 33 shows how this works: as the wing tilts for hover (top), its thrust vector moves forwards, so the box-wing thruster moment arm correctly extends forwards of the CG.

Both vehicles' center-of-gravity locations were estimated during post-processing, using a bottom-up approach in a spreadsheet. Results are in Table 13; they are defined relative to the vehicles' nose.

Table 13: Estimated center-of-gravity locations for the monoplane and box wing.

	Wingborne CG	Hover CG
Monoplane	47.7 cm	46.4 cm
Box wing	52.1 cm	49.4 cm

Table 13 shows that the CG locations are slightly different in wingborne flight and hover. This is because the nacelles and thrusters are in slightly different locations before vs. after they tilt. Also, the CG locations do not exactly correspond to the wing 50% chord position, as the optimizer assumes. Dimensional and thrust data is used to show (again in a spreadsheet) that the vehicles do indeed balance in hover. Results from the hover balance analysis are shown in Table 14.

Table 14: Results from the hover balance analysis.

	Monoplane		Box wing	
	Forward thrusters	Box-tail thruster	Box-wing thruster	Box-tail thruster
Hover thrust (total)	154.4 N	69.5 N	183.7 N	16.7 N
Thrust vector	-14.0 cm	180.4 cm	39.3 cm	160.1 cm
Moment arm	60.3 cm	-134.0 cm	10.1 cm	-110.7 cm
Moment	9315 N-cm	-9316 N-cm	1853 N-cm	-1853 N-cm
Net moment / moment	0.0%	0.0%	0.0%	0.0%

For each vehicle and thruster, Table 14 gives the hover thrust (from the optimizer) and thrust vector location (estimated geometrically). The moment arm is then the difference between the thrust vector and hover CG location (from Table 13). The moment is the product of the hover thrust and moment arm. Finally, the net moments sum to 0 for both vehicles, indicating that they balance in hover as required.

Note that the monoplane forward-thruster centroid in Table 14 is negative, indicating that it is located forwards of the nose. This can also be seen from Figure 35.

Appendix G Detailed dimensional data

Detailed dimensional data for the monoplane and box wing, taken directly from the optimization results, is given in Table 15 and Table 16 respectively. Note that number of thruster stages is approximated as a continuous variable, rather than as an integer.

Table 15: Dimensional data for the monoplane.

Parameter	Value
Overall length:	1.621 m
Overall wingspan:	2.214 m
Takeoff mass:	20.8 kg
Takeoff weight:	203.6 N
Wing loading:	42.2 kg/m^2
Empty mass fraction:	46.3%
Max power draw:	29.91 kW
Fuselage pod length:	0.810 m
Fuselage pod usable length:	0.344 m
Fuselage pod width:	0.290 m
Fuselage pod usable width:	0.178 m
Fuselage pod height:	0.259 m
Fuselage pod usable height:	0.152 m
Tail boom length:	1.135 m
Tail boom exposed length:	0.810 m
Tail boom diameter:	0.018 m
Tail boom wall thickness:	2.00 mm
Planar wing span:	2.214 m
Planar wing area:	0.492 m^2
Planar wing mean chord:	0.222 m
Planar wing root chord:	0.296 m
Planar wing tip chord:	0.148 m
Planar wing mean thickness:	45.7 mm
Planar wing aspect ratio:	9.96
Planar wing taper ratio:	0.5
Planar wing t/c ratio:	20.6%
Box tail chord:	0.281 m
Box tail width:	0.421 m
Box tail height:	0.421 m
Box tail total horizontal planform area:	0.237 m^2
Box tail total vertical planform area:	0.237 m^2
Box tail section t/c ratio:	10%
Forward booms length:	0.377 m
Forward booms diameter:	0.011 m
Forward booms wall thickness:	2.00 mm
Forward nacelles quantity:	2
Forward nacelles chord:	0.305 m
Forward nacelles width:	0.458 m
Forward nacelles height:	0.458 m
Forward nacelles total horizontal planform area:	0.279 m^2
Forward nacelles total vertical planform area:	0.279 m^2
Battery length:	0.115 m
Battery width:	0.178 m
Battery height:	0.152 m
Battery volume:	3115.7 cm^3
Battery energy capacity:	1495.5 Wh
Battery maximum power:	29.91 kW
HVPC maximum input power:	29.91 kW
HVPC maximum output power:	25.42 kW
Box-tail thruster number of stages:	19.5
Box-tail thruster gap spacing:	10.0 mm
Box-tail thruster stage length:	0.012 m
Box-tail thruster duct length:	0.234 m
Box-tail thruster total length:	0.281 m

Box-tail thruster duct cross-sectional area:	0.177 m^2
Box-tail thruster exit cross-sectional area:	0.177 m^2
Box-tail thruster exit area ratio:	1.0
Forward thrusters quantity:	2
Forward thrusters number of stages:	21.2

Forward thrusters gap spacing:	10.0 mm
Forward thrusters stage length:	0.012 m
Forward thrusters duct length:	0.254 m
Forward thrusters total length:	0.305 m
Forward thrusters duct cross-sectional area:	0.209 m^2
Forward thrusters exit cross-sectional area:	0.209 m^2
Forward thrusters exit area ratio:	1.0

Table 16: Dimensional data for the box wing.

Parameter	Value
Overall length:	1.508 m
Overall wingspan:	1.602 m
Takeoff mass:	18.6 kg
Takeoff weight:	182.2 N
Wing loading:	24.1 kg/m^2
Empty mass fraction:	45.7%
Max power draw:	26.77 kW
Fuselage pod length:	0.872 m
Fuselage pod usable length:	0.332 m
Fuselage pod width:	0.283 m
Fuselage pod usable width:	0.178 m
Fuselage pod height:	0.253 m
Fuselage pod usable height:	0.152 m
Tail boom length:	1.508 m
Tail boom exposed length:	0.636 m
Tail boom diameter:	0.011 m
Tail boom wall thickness:	2.00 mm
Box wing planform area:	0.772 m^2
Planar wing span:	1.602 m
Planar wing area:	0.386 m^2
Planar wing mean chord:	0.241 m
Planar wing root chord:	0.242 m
Planar wing tip chord:	0.240 m
Planar wing mean thickness:	40.7 mm
Planar wing aspect ratio:	6.64
Planar wing taper ratio:	1.0
Planar wing t/c ratio:	16.9%
Wing vertical section span:	0.360 m
Wing vertical section area:	0.086 m^2
Wing vertical section chord:	0.240 m
Wing vertical section t/c ratio:	16.9%
Box tail chord:	0.209 m
Box tail width:	0.314 m
Box tail height:	0.186 m
Box tail total horizontal planform area:	0.132 m^2
Box tail total vertical planform area:	0.078 m^2
Box tail section t/c ratio:	10%
Battery length:	0.103 m
Battery width:	0.178 m
Battery height:	0.152 m
Battery volume:	2788.4 cm^3
Battery energy capacity:	1338.5 Wh
Battery maximum power:	26.77 kW
HVPC maximum input power:	26.77 kW
HVPC maximum output power:	22.75 kW
Box-tail thruster number of stages:	14.5
Box-tail thruster gap spacing:	10.0 mm
Box-tail thruster stage length:	0.012 m
Box-tail thruster duct length:	0.175 m
Box-tail thruster total length:	0.209 m
Box-tail thruster duct cross-sectional area:	0.058 m^2
Box-tail thruster exit cross-sectional area:	0.058 m^2
Box-tail thruster exit area ratio:	1.0
Box-wing thruster number of stages:	16.7
Box-wing thruster gap spacing:	10.0 mm
Box-wing thruster stage length:	0.012 m
Box-wing thruster duct length:	0.201 m
Box-wing thruster total length:	0.241 m
Box-wing thruster duct cross-sectional area:	0.576 m^2
Box-wing thruster exit cross-sectional area:	0.576 m^2
Box-wing thruster exit area ratio:	1.0

Appendix H Mass breakdowns

Mass breakdowns for the monoplane and box wing, taken directly from the optimization results, are given in Table 17 and Table 18 respectively.

Table 17: Mass breakdown for the monoplane.

Component	Mass (kg)	Mass / Total (-)
Fuselage pod	0.47	2.2%
Tail boom	0.41	2.0%
Wing	1.10	5.3%
Box tail	0.67	3.2%
Forward nacelles	0.91	4.4%
Forward booms	0.16	0.8%
Landing gear	0.76	3.6%
Payload	1.20	5.8%
Payload mount	0.30	1.4%
Battery	7.48	36.0%
Power converter	2.46	11.9%
Box-tail thruster	0.49	2.4%
Forward thrusters	1.27	6.1%
Box-tail thruster tilting mechanism	0.29	1.4%
Forward thrusters tilting mechanism	0.54	2.6%
Avionics	0.38	1.8%
Margin	1.89	9.1%
Total	20.76	100.0%

Table 18: Mass breakdown for the box wing.

Component	Mass (kg)	Mass / Total (-)
Fuselage pod	0.49	2.6%
Tail boom	0.32	1.7%
Wing	1.98	10.7%
Box tail	0.26	1.4%
Landing gear	0.68	3.6%
Payload	1.20	6.5%
Payload mount	0.30	1.6%
Battery	6.69	36.0%
Power converter	2.20	11.9%
Box-tail thruster	0.12	0.7%
Box-wing thruster	1.38	7.4%
Box-wing thruster tilting mechanism	0.84	4.5%
Box-tail thruster tilting mechanism	0.09	0.5%
Avionics	0.34	1.8%
Margin	1.69	9.1%
Total	18.58	100.0%

Appendix I Detailed performance data

Time, distance travelled, and battery energy consumed, for each aircraft and mission segment, is provided in Table 19. This data was taken directly from the optimization results.

Table 19: Mission segment time, distance travelled, and battery energy consumed.

Mission segment	Monoplane			Box wing		
	Time (s)	Distance (km)	Battery energy (Wh)	Time (s)	Distance (km)	Battery energy (Wh)
Takeoff	5.0	n/a	41.5	5.0	n/a	37.2
Climb	1.0	0.0	2.4	1.0	0.0	2.1
Cruise out	392.6	10.0	609.4	396.2	10.0	547.5
Payload drop	20.0	n/a	166.2	20.0	n/a	148.7
Turn around	14.1	0.4	25.2	10.7	0.2	18.2
Cruise in	392.6	10.0	609.4	396.2	10.0	547.5
Landing	5.0	n/a	41.5	5.0	n/a	37.2

Detailed performance data, broken down by mission segment, is provided in Table 20 and Table 21 for the monoplane and box wing respectively. Note that the payload mass is not deducted from the aircraft mass after the payload drop, as the vehicle needs to be able to return with the payload if necessary. Therefore, all three hover segments (takeoff, payload drop, and landing) yield identical performance data. The same is true for both cruise segments (cruise out and cruise in).

Table 20: Performance data by mission segment for the monoplane.

Mission Segment	Hover	Climb	Cruise	Bank	Units
Airspeed	n/a	25.5	25.5	25.5	m/s
Lift coefficient	n/a	1.04	1.04	1.20	-
Profile drag coefficient	n/a	492.9	492.9	514.8	Counts
Induced drag coefficient	n/a	433.3	433.3	577.7	Counts
Margin drag coefficient	n/a	92.6	92.6	109.3	Counts
Total drag coefficient	n/a	1018.9	1018.9	1201.8	Counts
Lift-to-drag ratio	n/a	10.2	10.2	10.0	-
Thrust (total)	224.0	32.1	19.9	23.5	N
Thrust (box-tail thruster)	69.5	10.1	6.4	7.5	N
Thrust (forward thrusters)	154.4	22.0	13.5	16.0	N
Thrust per thruster (box-tail thruster)	69.5	10.1	6.4	7.5	N
Thrust per thruster (forward thrusters)	77.2	11.0	6.8	8.0	N
Power (battery)	29.91	8.52	5.59	6.41	kW
Power (HVPC)	25.42	7.24	4.75	5.45	kW
Power (box-tail thruster)	8.24	2.29	1.50	1.73	kW

Power (forward thrusters)	17.18	4.96	3.25	3.73	kW
Power per thruster (box-tail thruster)	8.24	2.29	1.50	1.73	kW
Power per thruster (forward thrusters)	8.59	2.48	1.62	1.86	kW
Voltage (box-tail thruster)	10.00	6.02	5.14	5.41	kV
Voltage (forward thrusters)	9.31	5.65	4.81	5.07	kV
Thrust-to-power (box-tail thruster)	8.44	4.42	4.26	4.34	N/kW
Thrust-to-power (forward thrusters)	8.99	4.44	4.16	4.29	N/kW
Thrust density (box-tail thruster)	391.9	57.0	36.1	42.3	N/m^2
losses due to wall friction	3.3	7.1	6.8	6.9	N/m^2
Thrust density (forward thrusters)	368.9	52.5	32.3	38.2	N/m^2
losses due to wall friction	3.1	6.9	6.7	6.7	N/m^2
Power density (box-tail thruster)	46.44	12.90	8.48	9.73	kW/m^2
ionization	0.30	0.14	0.11	0.12	kW/m^2
acceleration	46.14	12.76	8.37	9.61	kW/m^2
Power density (forward thrusters)	41.05	11.84	7.75	8.90	kW/m^2
ionization	0.29	0.14	0.10	0.11	kW/m^2
acceleration	40.76	11.70	7.65	8.79	kW/m^2
Bulk velocity (box-tail thruster)	18.0	27.4	26.8	27.0	m/s
Bulk velocity (forward thrusters)	17.4	27.3	26.7	26.8	m/s
Exit velocity (box-tail thruster)	18.0	27.4	26.8	27.0	m/s
Exit velocity (forward thrusters)	17.4	27.3	26.7	26.8	m/s
Current density (box-tail thruster)	236.6	108.7	83.6	91.1	mA/m^2
Current density (forward thrusters)	206.6	97.9	75.1	81.9	mA/m^2
Total current (box-tail thruster)	42.0	19.3	14.8	16.2	mA
Total current (forward thrusters)	43.3	20.5	15.7	17.1	mA
Current per thruster (box-tail thruster)	42.0	19.3	14.8	16.2	mA
Current per thruster (forward thrusters)	21.6	10.2	7.9	8.6	mA
Stage EAD pressure rise (box-tail thruster)	10.53	4.09	3.03	3.34	Pa
Stage EAD pressure rise (forward thrusters)	9.15	3.62	2.67	2.95	Pa
Stage electrode losses (box-tail thruster)	0.40	0.92	0.88	0.89	Pa
Stage electrode losses (forward thrusters)	0.37	0.91	0.87	0.88	Pa

Total pressure rise (box-tail thruster)	197.6	61.9	41.9	47.8	Pa
Total pressure rise (forward thrusters)	186.0	57.5	38.1	43.8	Pa

Table 21: Performance data by mission segment for the box wing.

Mission Segment	Hover	Climb	Cruise	Bank	Units
Segment distance	n/a	0.0	10.0	0.2	km
Segment battery energy	133.8	7.5	1971.1	65.5	kJ
Airspeed	n/a	23.2	25.2	19.2	m/s
Lift coefficient	n/a	0.71	0.60	1.20	-
Profile drag coefficient	n/a	237.1	229.6	274.0	Counts
Induced drag coefficient	n/a	447.0	321.8	1272.9	Counts
Margin drag coefficient	n/a	68.4	55.1	154.7	Counts
Total drag coefficient	n/a	752.6	606.6	1701.6	Counts
Lift-to-drag ratio	n/a	9.5	10.0	7.1	-
Thrust (total)	200.4	31.2	18.3	29.8	N
Thrust (box-tail thruster)	16.7	2.5	1.4	2.4	N
Thrust (box-wing thruster)	183.7	28.7	16.8	27.4	N
Power (battery)	26.77	7.54	4.98	6.14	kW
Power (HVPC)	22.75	6.41	4.23	5.22	kW
Power (box-tail thruster)	1.93	0.57	0.39	0.46	kW
Power (box-wing thruster)	20.83	5.84	3.84	4.76	kW
Voltage (box-tail thruster)	9.92	6.12	5.24	5.77	kV
Voltage (box-wing thruster)	9.72	5.89	4.98	5.57	kV
Thrust-to-power (box-tail thruster)	8.69	4.42	3.71	5.26	N/kW
Thrust-to-power (box-wing thruster)	8.82	4.91	4.38	5.74	N/kW
Thrust density (box-tail thruster)	287.1	43.0	24.6	41.4	N/m^2
losses due to wall friction	3.6	8.6	9.4	6.3	N/m^2
Thrust density (box-wing thruster)	318.8	49.8	29.2	47.5	N/m^2
losses due to wall friction	2.1	4.5	5.0	3.4	N/m^2
Power density (box-tail thruster)	33.04	9.73	6.61	7.88	kW/m^2
ionization	0.22	0.10	0.08	0.09	kW/m^2
acceleration	32.82	9.63	6.53	7.79	kW/m^2
Power density (box-wing thruster)	36.15	10.14	6.67	8.26	kW/m^2
ionization	0.24	0.11	0.09	0.10	kW/m^2
acceleration	35.90	10.03	6.58	8.17	kW/m^2
Bulk velocity (box-tail thruster)	15.4	24.9	26.3	21.1	m/s
Bulk velocity (box-wing thruster)	16.2	25.0	26.3	21.2	m/s

Exit velocity (box-tail thruster)	15.4	24.9	26.3	21.1	m/s
Exit velocity (box-wing thruster)	16.2	25.0	26.3	21.2	m/s
Current density (box-tail thruster)	227.5	108.1	85.6	92.8	mA/m^2
Current density (box-wing thruster)	220.7	101.7	79.0	87.6	mA/m^2
Total current (box-tail thruster)	13.3	6.3	5.0	5.4	mA
Total current (box-wing thruster)	127.2	58.6	45.5	50.5	mA
Stage EAD pressure rise (box-tail thruster)	10.28	4.19	3.14	3.68	Pa
Stage EAD pressure rise (box-wing thruster)	9.90	3.90	2.85	3.45	Pa
Stage electrode losses (box-tail thruster)	0.29	0.76	0.85	0.54	Pa
Stage electrode losses (box-wing thruster)	0.32	0.77	0.85	0.55	Pa
Total pressure rise (box-tail thruster)	145.4	49.8	33.3	45.7	Pa
Total pressure rise (box-wing thruster)	160.4	52.4	33.5	48.5	Pa

References

[1] L. A. Garrow *et al.*, "A Proposed Taxonomy for Advanced Air Mobility," presented at the AIAA Aviation Forum, Chicago, IL, Jun. 2022, pp. 1–25. doi: 10.2514/6.2022-3321.

[2] "Google Wing: how it works," *Wing*. https://wing.com/how-it-works/ (accessed Sep. 22, 2022).

[3] "Amazon Prime Air prepares for drone deliveries," *About Amazon*, Jun. 13, 2022. https://www.aboutamazon.com/news/transportation/amazon-prime-air-prepares-for-drone-deliveries (accessed Oct. 17, 2022).

[4] N. Boysen, S. Fedtke, and S. Schwerdfeger, "Last-mile delivery concepts: a survey from an operational research perspective," *OR Spectrum*, vol. 43, no. 1, pp. 1–58, Mar. 2021, doi: 10.1007/s00291-020-00607-8.

[5] M. Elsayed and M. Mohamed, "The impact of airspace regulations on unmanned aerial vehicles in last-mile operation," *Transportation Research Part D: Transport and Environment*, vol. 87, p. 102480, Oct. 2020, doi: 10.1016/j.trd.2020.102480.

[6] J. K. Stolaroff, C. Samaras, E. R. O'Neill, A. Lubers, A. S. Mitchell, and D. Ceperley, "Energy use and life cycle greenhouse gas emissions of drones for commercial package delivery," *Nat Commun*, vol. 9, no. 1, Art. no. 1, Feb. 2018, doi: 10.1038/s41467-017-02411-5.

[7] P. D. Vascik and R. J. Hansman, "Scaling Constraints for Urban Air Mobility Operations: Air Traffic Control, Ground Infrastructure, and Noise," presented at the 2018 Aviation Technology, Integration, and Operations Conference, Atlanta, GA, 2018, pp. 1–26. doi: 10.2514/6.2018-3849.

[8] D. Y. Gwak, D. Han, and S. Lee, "Sound quality factors influencing annoyance from hovering UAV," *Journal of Sound and Vibration*, vol. 489, 2020, doi: 10.1016/j.jsv.2020.115651.

[9] J. Gothe-Snape, "Google-affiliated drone delivery service found to be exceeding noise limits," *ABC News*, Sep. 11, 2019. https://www.abc.net.au/news/2019-09-12/canberra-delivery-drone-noise-levels-revealed/11503262 (accessed Oct. 17, 2022).

[10] S. Robinson, "'Do it somewhere else': Glendale residents asking Walmart to stop drone delivery service," *Arizona's Family*, Jan. 06, 2023. https://www.azfamily.com/video/2023/01/07/glendale-residents-asking-walmart-stop-drone-deliveries/ (accessed Feb. 01, 2023).

[11] A. Synodinos, R. Self, and A. Torija, "Preliminary Noise Assessment of Aircraft with Distributed Electric Propulsion," presented at the 2018 AIAA/CEAS Aeroacoustics Conference, Atlanta, GA, 2018, pp. 1–21. doi: 10.2514/6.2018-2817.

[12] E. A. Christenson and P. S. Moller, "Ion-Neutral Propulsion in Atmospheric Media," *AIAA Journal*, vol. 5, no. 10, pp. 1768–1773, 1967, doi: 10.2514/3.4302.

[13] L. Pekker and M. Young, "Model of Ideal Electrohydrodynamic Thruster," *Journal of Propulsion and Power*, vol. 27, no. 4, pp. 786–792, Jul. 2011, doi: 10.2514/1.b34097.

[14] K. Masuyama and S. R. H. Barrett, "On the performance of electrohydrodynamic propulsion," *Proceedings of the Royal Society A: Mathematical, Physical and Engineering Sciences*, vol. 469, no. 2154, p. 20120623, 2013, doi: 10.1098/rspa.2012.0623.

[15] C. K. Gilmore and S. R. H. Barrett, "Electrohydrodynamic thrust density using positive corona-induced ionic winds for in-atmosphere propulsion," *Proceedings of the Royal Society A: Mathematical, Physical and Engineering Sciences*, vol. 471, no. 2175, p. 20140912, 2015, doi: 10.1098/rspa.2014.0912.

[16] H. Xu *et al.*, "Flight of an aeroplane with solid-state propulsion," *Nature*, vol. 563, no. 7732, pp. 532–535, 2018, doi: 10.1038/s41586-018-0707-9.

[17] H. Xu, Y. He, and S. R. H. Barrett, "A dielectric barrier discharge ion source increases thrust and efficiency of electroaerodynamic propulsion," *Applied Physics Letters*, vol. 114, no. 25, p. 254105, Jun. 2019, doi: 10.1063/1.5100524.

[18] X. Huang and X. Zhang, "Plasma Actuators for Noise Control," *Aeroacoustics*, vol. 9, no. 4 & 5, pp. 679–704, Jun. 2020, doi: https://doi.org/10.1260/1475-472X.9.4-5.67.

[19] Y. He, M. Woolston, and D. Perreault, "Design and implementation of a lightweight high-voltage power converter for electro-aerodynamic propulsion," presented at the 2017 IEEE 18th Workshop on Control and Modeling for Power Electronics (COMPEL), Jul. 2017, pp. 1–9. doi: 10.1109/COMPEL.2017.8013315.

[20] N. Gomez-Vega, A. Brown, H. Xu, and S. R. H. Barrett, "Model of Multistaged Ducted Thrusters for High-Thrust-Density Electroaerodynamic Propulsion," *AIAA Journal*, vol. 61, no. 2, pp. 767–779, Feb. 2023, doi: 10.2514/1.J061948.

[21] G. Warwick, "The Week In Technology, June 20-24, 2022 | Aviation Week Network," Jun. 20, 2022. https://aviationweek.com/aerospace/week-technology-june-20-24-2022?elq2=fe0d29ce60404ae287d0937da2ddc7be&sp_eh=b3374dfbe97fe67b4c3beb636192f3726cf2e89c0eebff51c036607de9a6ee41&utm_campaign=33384&utm_emailname=AW_News_Aerospace_20220620&utm_medium=email&utm_rid=CPEN1000003329014 (accessed Sep. 22, 2022).

[22] "Choice 20 oz. White Poly Paper Hot Cup and Lid - 100/Pack," *WebstaurantStore*. https://www.webstaurantstore.com/choice-20-oz-white-poly-paper-hot-cup-and-lid-pack/99920W100.html (accessed Oct. 12, 2022).

[23] L. Getson, "Take-Out Packaging Buying Guide," *CiboWares*, May 18, 2017. https://cibowares.com/blogs/news/take-out-packaging-buying-guide (accessed Oct. 12, 2022).

[24] D. P. Raymer, *Aircraft design: a conceptual approach*, 5th ed. Reston, VA: American Institute of Aeronautics and Astronautics, 2012.

[25] R. A. McDonald and J. R. Gloudemans, "Open Vehicle Sketch Pad: An Open Source Parametric Geometry and Analysis Tool for Conceptual Aircraft Design," presented at the AIAA SciTech Forum, San Diego, CA, Jan. 2022. doi: 10.2514/6.2022-0004.

[26] P. G. Kirschen and W. W. Hoburg, "The Power of Log Transformation: A Comparison of Geometric and Signomial Programming with General Nonlinear Programming Techniques for Aircraft Design Optimization," presented at the 2018 AIAA/ASCE/AHS/ASC

Structures, Structural Dynamics, and Materials Conference, Kissimmee, FL, 2018, pp. 1–11. doi: doi:10.2514/6.2018-0655.

[27] W. Hoburg and P. Abbeel, "Geometric Programming for Aircraft Design Optimization," *AIAA Journal*, vol. 52, no. 11, pp. 2414–2426, 2014, doi: 10.2514/1.J052732.

[28] M. Burton and W. Hoburg, "Solar and Gas Powered Long-Endurance Unmanned Aircraft Sizing via Geometric Programming," *Journal of Aircraft*, vol. 55, no. 1, pp. 212–225, 2018, doi: 10.2514/1.C034405.

[29] A. Brown and W. L. Harris, "Vehicle Design and Optimization Model for Urban Air Mobility," *Journal of Aircraft*, vol. 57, no. 6, pp. 1003–1013, Nov. 2020, doi: 10.2514/1.c035756.

[30] A. R. Gnadt, S. Isaacs, R. Price, M. Dethy, and C. Chappelle, "Hybrid Turbo-Electric STOL Aircraft for Urban Air Mobility," presented at the AIAA SciTech 2019 Forum, San Diego, CA, 2019, pp. 1–22. doi: 10.2514/6.2019-0531.

[31] C. Courtin and R. J. Hansman, "Model Development for a Comparison of VTOL and STOL Electric Aircraft Using Geometric Programming," presented at the AIAA Aviation 2019 Forum, Dallas, TX, Jun. 2019, pp. 1–18. doi: https://doi.org/10.2514/6.2019-3477.

[32] P. G. Kirschen, M. A. York, B. Ozturk, and W. W. Hoburg, "Application of Signomial Programming to Aircraft Design," *Journal of Aircraft*, vol. 55, no. 3, pp. 1–23, May 2018, doi: 10.2514/1.C034378.

[33] D. K. Hall, A. Dowdle, J. Gonzalez, L. Trollinger, and W. Thalheimer, "Assessment of a Boundary Layer Ingesting Turboelectric Aircraft Configuration using Signomial Programming," presented at the 2018 Aviation Technology, Integration, and Operations Conference, Atlanta, GA, 2018, pp. 1–16. doi: 10.2514/6.2018-3973.

[34] D. Chandel *et al.*, "Conceptual Design of Distributed Electrified Boundary Layer Ingesting Propulsors for the CHEETA Aircraft Concept," presented at the AIAA Propulsion and Energy Forum, 2021, pp. 1–16. doi: 10.2514/6.2021-3287.

[35] A. P. Dowdle, D. K. Hall, and J. H. Lang, "Electric Propulsion Architecture Assessment via Signomial Programming," presented at the 2018 AIAA/IEEE Electric Aircraft Technologies Symposium, Cincinnati, OH, Jul. 2018, pp. 1–23. doi: https://doi.org/10.2514/6.2018-5026.

[36] L. G. Hector and H. L. Schultz, "The Dielectric Constant of Air at Radiofrequencies," *Physics*, vol. 7, no. 4, pp. 133–136, Apr. 1936, doi: 10.1063/1.1745374.

[37] S. Coseru, D. Fabre, and F. Plouraboué, "Numerical study of ElectroAeroDynamic force and current resulting from ionic wind in emitter/collector systems," *Journal of Applied Physics*, vol. 129, no. 10, p. 103304, Mar. 2021, doi: 10.1063/5.0041061.

[38] N. Gomez-Vega, H. Xu, J. M. Abel, and S. R. H. Barrett, "Performance of decoupled electroaerodynamic thrusters," *Applied Physics Letters*, vol. 118, no. 7, p. 074101, Feb. 2021, doi: 10.1063/5.0038208.

[39] S. Sripad and V. Viswanathan, "The promise of energy-efficient battery-powered urban aircraft," *Proceedings of the National Academy of Sciences*, vol. 118, no. 45, p. e2111164118, Oct. 2021, doi: https://doi.org/10.1073/pnas.2111164118.

[40] M. Drela, “XFOIL: An Analysis and Design System for Low Reynolds Number Airfoils,” in *Low Reynolds Number Aerodynamics*, Berlin, Heidelberg, 1989, pp. 1–12. doi: 10.1007/978-3-642-84010-4_1.

[41] Mark Drela, “Wing Bending Calculations (Lab 10 Lecture Notes),” MIT OpenCourseWare, 2006. Accessed: Oct. 19, 2022. [Online]. Available: https://ocw.mit.edu/courses/16-01-unified-engineering-i-ii-iii-iv-fall-2005-spring-2006/c5f687b07f1a376a5c785aab490c06ef_spl10.pdf

[42] S. Macheret, M. Shneider, and R. Miles, “Modeling of air plasma generation by electron beams and high-voltage pulses,” in *31st Plasmadynamics and Lasers Conference*, American Institute of Aeronautics and Astronautics, 2000. doi: 10.2514/6.2000-2569.

[43] Y. P. Raizer, *Gas Discharge Physics*. Berlin: Springer-Verlag, 1991.

[44] H. Xu, “Experiments in Electroaerodynamic Propulsion,” PhD Thesis, Massachusetts Institute of Technology, 2020.

[45] T. Orrière, É. Moreau, and D. Z. Pai, “Electric wind generation by nanosecond repetitively pulsed microplasmas,” *J. Phys. D: Appl. Phys.*, vol. 52, no. 46, p. 464002, Sep. 2019, doi: 10.1088/1361-6463/ab372f.

[46] C. L. Allen and A. R. Taylor, “Negative ion generator using an ultraviolet source to irradiate electrically conductive material,” US3128378A, Apr. 07, 1964 Accessed: Jan. 30, 2023. [Online]. Available: https://patents.google.com/patent/US3128378A/en

[47] “Nitrogen,” *Chemistry WebBook, National Institute of Standards and Technology*, 2021. https://webbook.nist.gov/cgi/cbook.cgi?ID=C7727379&Mask=20 (accessed Jan. 30, 2023).

[48] A. Korobenko *et al.*, “In-Situ Nanoscale Focusing of Extreme Ultraviolet Solid-State High Harmonics,” *Phys. Rev. X*, vol. 12, no. 4, p. 041036, Dec. 2022, doi: 10.1103/PhysRevX.12.041036.

[49] A. González, “1.5 X-Ray Crystallography: Data Collection Strategies and Resources,” in *Comprehensive Biophysics*, E. H. Egelman, Ed. Amsterdam: Elsevier, 2012, pp. 64–91. doi: 10.1016/B978-0-12-374920-8.00106-5.

[50] “Cross Sections for Collisions of Electrons and Photons with Nitrogen Molecules: Journal of Physical and Chemical Reference Data: Vol 15, No 3.” https://aip.scitation.org/doi/abs/10.1063/1.555762 (accessed Jan. 30, 2023).

[51] V. P. Guinn, “Radioactivity,” in *Encyclopedia of Physical Science and Technology (Third Edition)*, R. A. Meyers, Ed. New York: Academic Press, 2003, pp. 661–674. doi: 10.1016/B0-12-227410-5/00643-8.

[52] K. Kostecka, “Americium - from discovery to the smoke detector and beyond,” *Bulletin for the History of Chemistry*, vol. 33, no. 2, pp. 89–93, 2008.

[53] R. C. O’Brien, R. M. Ambrosi, N. P. Bannister, S. D. Howe, and H. V. Atkinson, “Safe radioisotope thermoelectric generators and heat sources for space applications,” *Journal of Nuclear Materials*, vol. 377, no. 3, pp. 506–521, Jul. 2008, doi: 10.1016/j.jnucmat.2008.04.009.

[54] W. Hoburg, P. Kirschen, and P. Abbeel, “Data fitting with geometric-programming-compatible softmax functions,” *Optimization and Engineering*, 2016, doi: 10.1007/s11081-016-9332-3.

[55] H. Schlichting and K. Gersten, *Boundary-Layer Theory*, 9th ed. Springer Berlin Heidelberg, 2016. doi: 10.1007/978-3-662-52919-5.

[56] “Tungsten-Re3% Wire .0003".” https://espimetals.com/shop/tungsten-re3-wire-0003.html (accessed Jan. 27, 2023).

[57] V. Jain, U. Dixit, C. Paul, and A. Kumar, “Micromanufacturing: A review—part II,” *Proceedings of the Institution of Mechanical Engineers, Part B: Journal of Engineering Manufacture*, vol. 228, no. 9, pp. 995–1014, Sep. 2014, doi: 10.1177/0954405414539492.

[58] Y. Qin, *Micromanufacturing Engineering and Technology*, 2nd ed. Elsevier Inc., 2015.

[59] M. A. Teplechuk, F. Banag, B. Mcadam, T. Gribben, and Z. Mengad, “A 7.8W continuous and 19.6W burst output power fully integrated 2S Class-D amplifier with 0.005% THD+N,” in *2016 IEEE 7th Latin American Symposium on Circuits & Systems (LASCAS)*, Feb. 2016, pp. 35–38. doi: 10.1109/LASCAS.2016.7451003.

[60] J. M. Rheaume and C. Lents, “Energy Storage for Commercial Hybrid Electric Aircraft,” in *SAE Technical Papers*, Sep. 2016, vol. 2016-Septe, no. September. doi: 10.4271/2016-01-2014.

[61] “Battery Modules - Driving Efficiency Speed to Market,” *A123 Systems*. http://www.a123systems.com/automotive/products/modules/ (accessed Jan. 30, 2023).

[62] A. Brown and W. L. Harris, “A Vehicle Design and Optimization Model for On-Demand Aviation,” presented at the 2018 AIAA/ASCE/AHS/ASC Structures, Structural Dynamics, and Materials Conference, Kissimmee, Florida, Jan. 2018. doi: 10.2514/6.2018-0105.

[63] F. Fahy and D. Thompson, *Fundamentals of Sound and Vibration*. CRC Press, 2015.

[64] H. Xu, N. Gomez-Vega, D. R. Agrawal, and S. R. H. Barrett, “Higher thrust-to-power with large electrode gap spacing electroaerodynamic devices for aircraft propulsion,” *Journal of Physics D: Applied Physics*, Oct. 2019, doi: 10.1088/1361-6463/ab4a4c.

[65] D. Schiktanz and D. Scholz, “Box Wing Fundamentals - an Aircraft Design Perspective,” presented at the German Aerospace Conference, Bremen, Germany, 2011, pp. 601–615.

[66] Aldo Frediani and Guido Montanari, “Best Wing System - An Exact Solution of the Prandtl’s Problem,” in *Variational Analysis and Aerospace Engineering*, New York, NY, 2009, vol. 33. doi: 10.1007/978-0-387-95857-6.

[67] M. Nita and D. Scholz, “Estimating the Oswald Factor from Basic Aircraft Geometrical Parameters,” *Deutscher Luft- und Raumfahrtkongress*, vol. 281424, pp. 1–19, 2012.